

White Dwarfs in the SuperCOSMOS Sky Survey: the Thin Disk, Thick Disk and Spheroid Luminosity Functions

N. Rowell^{1*} and N. C. Hambly²

¹*Space Technology Centre, School of Computing,
University of Dundee, Dundee, DD1 4HN*

²*Scottish Universities Physics Alliance (SUPA), Institute for Astronomy,
School of Physics and Astronomy, University of Edinburgh,
Royal Observatory, Blackford Hill, Edinburgh EH9 3HJ*

Accepted xx.xx.xxxx. Received xx.xx.xxxx; in original form xx.xx.xxxx

ABSTRACT

We present a magnitude and proper motion limited catalogue of $\sim 10,000$ white dwarf candidates, obtained from the SuperCOSMOS Sky Survey by means of reduced proper motion selection. This catalogue extends to magnitudes $R \sim 19.75$ and proper motions as low as $\mu \sim 0''.05 \text{ yr}^{-1}$, and covers nearly three quarters of the sky. Photometric parallaxes provide distance estimates accurate to $\sim 50\%$. This catalogue is used to measure the luminosity functions for disk and spheroid white dwarfs, using strict velocity cuts to isolate subsamples belonging to each population. Disk luminosity functions measured in this manner are really a conglomerate of thin and thick disk objects, due to the significant velocity overlap between these populations. We introduce a new statistical approach to the stellar luminosity function for nearby objects that successfully untangles the contributions from the different kinematic populations, without the need for stringent velocity cuts. This improves the statistical power by allowing all stars to contribute to the luminosity function, even at tangential velocities where the populations are indistinguishable. This method is particularly suited to white dwarfs, for which population discrimination by chemical tagging is not possible. We use this technique to obtain the first measurement of the thick disk white dwarf luminosity function, while also improving constraint on both the thin disk and spheroid luminosity functions. We find that the thin disk, thick disk and spheroid populations contribute to the local white dwarf density in roughly 79%/16%/5% proportions.

Key words: White dwarfs; stars: luminosity function, mass function; surveys; Solar neighbourhood.

1 INTRODUCTION

Nearly all stars in the Galaxy will end their lives as faint white dwarfs (WDs), once nuclear burning has ceased and the outer photospheric layers have been ejected. The further evolution of these objects is a gradual cooling process, where the remaining thermal energy of the exposed core is slowly radiated away through the thin outer layers. WDs are highly numerous in the Solar neighbourhood. They are the second most common type of star behind low mass main sequence stars, but due to their extreme faintness are found in much smaller numbers in Galactic star surveys. As a result, the evolution of the coolest WDs is rather poorly constrained observationally (Hansen & Liebert 2003; Gates et al. 2004; Vidrih et al. 2007; Rowell et al. 2008; Kilic et al. 2010), and

though much work has been done on the theoretical front in recent years (Fontaine et al. 2001; Bergeron et al. 2001) it is still unclear how to interpret the small amount of observational evidence available (e.g. Bergeron & Leggett 2002; Bedin et al. 2008). Studies of the luminosity function for white dwarfs (WDLF) typically focus on the faint end, where the finite age of the Galaxy predicts a sudden downturn in the local density of WDs when the cooling times converge on the age of the population as a whole. The first evidence for this was published by Liebert et al. (1988), and was used by Winget et al. (1987) to obtain an estimate of the age of the universe essentially independent of main sequence stellar ages. Although many more studies have been carried out in the intervening decades, focussing on both the Galactic disk (Oswalt et al. 1996; Leggett et al. 1998; Knox et al. 1999) and clusters (Hansen et al. 2002; Bedin et al. 2010) it is the advent of digitized wide angle sky surveys in the last

* E-mail: nickrowell@computing.dundee.ac.uk

decade that has revolutionised the study of these objects in the field, with large footprint areas greatly increasing the survey volume for faint objects.

The Sloan Digital Sky Survey (SDSS) has provided the most interesting results in recent years. Several independent surveys have increased the catalogue of known WDs by more than an order of magnitude, providing greater statistical power at both the hot end of the LF, where the WDs are intrinsically rare, and the cool end where they exist in large number but are extremely faint. For example, Krzesinski et al. (2009) use colour selection to identify a few hundred hot WDs from the SDSS spectral catalogue. Their luminosity function extends to $M_{bol} = 7.0$, where the sample starts to become incomplete due to the selection probability for spectroscopic follow up dropping off at lower temperatures. Eisenstein et al. (2006) identified more than 9,000 spectroscopically confirmed WDs in SDSS DR4, and their catalogue was used by De Gennaro et al. (2008) to probe the WDLF for different WD mass ranges. As cool WDs are generally selected for SDSS spectroscopic follow-up by algorithms designed to target QSOs, the completeness of such a catalogue is a strong function of colour. Kilic et al. (2006) and Harris et al. (2006) (hereafter H06) used reduced proper motion to identify ~ 6000 WDs, with proper motions determined by pairing sources with the USNO-B catalogue. The reduced proper motion approach offers a superior survey method for a couple of reasons. First, it is insensitive to colour, and cool WDs can be identified among the highly numerous disk stars from which they are indistinguishable in colour space. Second, it provides a statistically rigorous selection probability, avoiding the need to calculate detailed completeness functions to prevent survey bias. The WDLF of H06 is currently the deepest and best constrained around the faint turnover in the disk LF, though the pairing criterion limits the depth of their catalogue to the magnitude limits of the USNO-B survey.

There has been considerable interest in Galactic spheroid WDs in the last decade, though very little is known about this elusive population of stars. Broad predictions can be made on the basis of Galactic formation and stellar evolution models, (e.g. Hansen 1999; Reid 2005) but the contribution made by these objects to the local density and Galactic mass budget is very poorly constrained. This is due to a combination of several factors. Firstly, these objects are both faint and intrinsically very rare, and in any given survey will be found in much smaller numbers than both disk WDs and other types of star. They are far too faint to be seen at large Galactic plane distances in regions of pure spheroid stars, and any objects must be observed as they pass through the nearby Galactic disk. They also cannot be identified by low metallicities, because for all WDs the surface gravity is high enough to pull metals below the photosphere. The only reliable way to identify them is by their large space velocities, as the high velocity tail of the distribution is cleanly separated from both the thin and thick disk (Vidrih et al. 2007; Kilic et al. 2010). This technique was used by H06 to measure the first luminosity function for spheroid WDs of any significant size.

The thin and thick disk WD populations overlap too much in velocity for single objects to be reliably attributed to either population. For this reason, there has never been a direct measurement of the thick disk WDLF, though all

previous measurements of the WDLF for thin disk stars will have contained a significant number of these objects. In this paper, we show that the thin and thick disk WDLFs can indeed be measured separately from a mixed catalogue, by avoiding the need to classify each survey object as one type or the other. This technique has more statistical power than the traditional approach, because all objects are allowed to contribute to the luminosity function, even at tangential velocities where the populations are indistinguishable.

This paper is organised as follows: in Section 2 we describe the source data and detail efforts to construct a complete catalogue of stars. In Section 3 we use proper motion survey techniques to obtain a subsample of WD candidates from our catalogue, and in Section 4 we review the catalogue with emphasis on the completeness and likely mixture of kinematic populations present. In Section 5 we describe the traditional $\frac{1}{V_{max}}$ approach to measuring the luminosity function from a proper motion catalogue, and in Section 6 we use this technique to measure luminosity functions for various velocity subsamples drawn from our WD catalogue. In Section 7 we present our statistical approach to separating the kinematic populations, and measure WDLFs for the thin disk, thick disk and spheroid. In Sections 8 and 9 we compare our results to those of other studies and draw our conclusions.

2 THE DATA

The SuperCOSMOS Sky Survey (SSS) was compiled by digitizing several generations of photographic Schmidt plate surveys. The source material includes the second generation POSSII-*B, R, I* and SERC-*J/E/J, ER/AAO-R, I* surveys, observed by the Palomar Oschin Schmidt Telescope in the northern hemisphere and the United Kingdom Schmidt Telescope in the south. These were performed in the photographic *b_J r_{59F} i_N* bands. The subscripts refer to particular combinations of filter and photographic emulsion used by the surveys; we ignore the small differences in response between the northern and southern hemisphere.

The first generation POSSI-*E* and ESO-*R* surveys provide an early epoch for astrometric constraint. The photometry is mostly redundant due to a similar response to *r_{59F}*, but we will nevertheless refer to magnitudes in these surveys as *r_{103aE}* and *r_{63F}* when distinction has to be made. Note that *r_{103aE}* and *r_{63F}* are identical in response, but we do expect differences in the survey characteristics due to e.g. a different copying history prior to digitization. These surveys cross over at $\delta \sim -18^\circ$, thus the sky is divided into three regions of common photographic material. This has implications for the characteristics of the digitized survey. Over 1700 fields are required to cover the whole sky, with each field being observed in each of the four photographic bands to a depth of $r \sim 21$. The four observations in each field are spread over a wide time baseline in the latter half of the twentieth century, with up to fifty years between epochs in the extreme.

Schmidt plates were digitized by the SuperCOSMOS scanning machine, scanning at 0.67 arcsecond pixel size and 15 bit digitization. SuperCOSMOS was operated at the Royal Observatory of Edinburgh - see Hambly et al. (2001a) for an introduction to SuperCOSMOS and brief historical

census of scanning programs. In some cases, glass or film copies of survey plates were scanned rather than originals. This includes the entire northern hemisphere. The use of photographic copies was not thought to significantly degrade the quality of the scanned data, however we regard each of the surveys as having independent characteristics in case any differences arise. Image Analysis Mode software was used to process the raw pixel data into parameterised object catalogues, which were then merged across the four epochs to measure proper motion and colours.

The SSS data are housed in a relational database at the Wide Field Astronomy Unit, Royal Observatory of Edinburgh. The original SSS is now contained within the SuperCOSMOS Science Archive, with access provided via a web-based SQL query form at <http://surveys.roe.ac.uk/ssa/>. Parametrised object information is dispensed from two large tables; the `detection` table contains roughly 6.4 billion individual object detections, which are merged into around 1.9 billion multi-colour, multi-epoch observations in the `source` table. A comprehensive description, user-guide and technical notes for the SSS were released in a series of three papers - see Hambly et al. 2001a,b,c.

2.1 Proper motion limits

The input data for our proper motion survey is drawn from two sources. The online SSA provides low proper motion coverage, from a rough lower 5σ detection limit of $0''.05 \text{ yr}^{-1}$ to a fixed upper limit of $0''.18 \text{ yr}^{-1}$. The completeness of the SSA at this upper limit varies widely between fields, due to the differing epoch spread and fixed search radius for object pairing. Early tests revealed that fields start to become incomplete above around $0''.08 \text{ yr}^{-1}$, as indicated by a significant departure from the linear relation $\log(\Sigma N(> \mu)) \propto \log(\mu)$. Our low proper motion data is thus truncated at an upper limit of $0''.08 \text{ yr}^{-1}$, with lower limits set according to the procedure outlined in the following section.

Faster moving objects are recovered using a more sophisticated search algorithm described in Hambly et al. (2004). Object pairing between epochs works on a field-by-field basis, and starts with the complete set of parameterized object detections on each of the four plates. Any sources that have been successfully merged and included in the default SSS catalogue at motions lower than the $0''.08 \text{ yr}^{-1}$ limit are thrown away. The remaining objects are then paired in all possible combinations within a search radius set by the chosen upper proper motion limit of $10''.0 \text{ yr}^{-1}$ and the epoch difference between plates. The primary pairing is between the two r epochs, which are subject to a magnitude limit of $r_{59F} < 19.75$ to reduce noise, but any detections in b_J and i_N are folded into the analysis to improve the astrometric solution. To produce an all sky catalogue, we take the entire object catalogue and purge multiple observations appearing in plate overlap regions, keeping whichever appears closest to its respective field centre in order to match the seaming of the low proper motion catalogue. This is far more rigorous than the object pairing in the default SSS, and is designed to maximise completeness of high proper motion objects at the expense of introducing large numbers of spurious detections.

Appropriate selection of astrometric and image statistics is necessary to reduce the contamination to a tolerable level.

2.1.1 Low proper motion completeness limits

We impose a lower proper motion limit on a field-by-field basis such that all objects have at least a $5\sigma_\mu$ proper motion detection, defined by

$$\sigma_\mu = \sqrt{\left(\frac{\mu_\alpha \cos(\delta)}{\mu}\right)^2 \sigma_{\mu_\alpha \cos(\delta)}^2 + \left(\frac{\mu_\delta}{\mu}\right)^2 \sigma_{\mu_\delta}^2}$$

This excludes non-moving objects from our catalogue, and limits scatter in the reduced proper motion diagram that is used to select white dwarf candidates. However, we cannot simply select all objects with $\geq 5\sigma_\mu$ detections, because the proper motion errors show significant scatter at constant magnitude. The resulting survey volume limits at given tangential velocity would be unknown, as it would be impossible to measure the distance at which the star dropped below the required $5\sigma_\mu$ detection threshold. Therefore, we wish to find the *maximum* proper motion error as a function of magnitude, and use this to fix the lower proper motion limit. This guarantees that all objects that pass the limit also have $\geq 5\sigma_\mu$ detections. The proper motion error σ_μ varies from field to field, due to differences in plate quality and time baseline. It is also a strong function of magnitude, and at constant magnitude shows a significant spread. Figure 1(a) shows the distribution of σ_μ with b_J for a representative field. We use b_J in this analysis because it is the highest quality photometry available. Objects in the upper locus have been missed at one of the four epochs, usually r_{63F} , and have inferior astrometric fits. For this reason we restrict our low proper motion sample to objects with four plate detections. To fix the proper motion limit, we fit functions to the upper boundaries of the b_J, σ_μ locus. The procedure for each field is as follows. We start at the bright end of the distribution, and bin objects on magnitude interactively so that all bins contain one hundred objects. The mean b_J and maximum σ_μ in each bin is located, after rejecting the top 5% of σ_μ as outliers. The full set of $\langle b_J \rangle, \sigma_\mu^{max}$ points defines the rough upper boundary of the locus, but shows considerable noise on small scales. The raw fit is then processed through one stage of smoothing to obtain the desired function. We use a Savitzky-Golay technique to smooth the data, generalized from their original prescription (Savitzky & Golay 1964) to allow for non-uniform points on the abscissa. This removes small-scale noise while preserving any low-frequency features, such as the mid-magnitude turning point seen in most fields. Figure 1(b) shows the same field as (a), but restricted to four plate detections, and with the fitted functions shown. The final, smoothed function obtained for each field is denoted $\sigma_\mu^{max}(b_J)$, and is used to set the lower proper motion limit according to

$$\mu_{min}(b_J) = 5(\sigma_\mu^{max}(b_J) + 0''.002 \text{ yr}^{-1}).$$

The set of points defining $\sigma_\mu^{max}(b_J)$ is tabulated for each field, and interpolated using cubic splines to obtain the proper motion limit at arbitrary apparent magnitude. Thus the lower proper motion limit is a piecewise function of apparent magnitude, which complicates the measurement of the survey volume, but maximises the sample size by fully

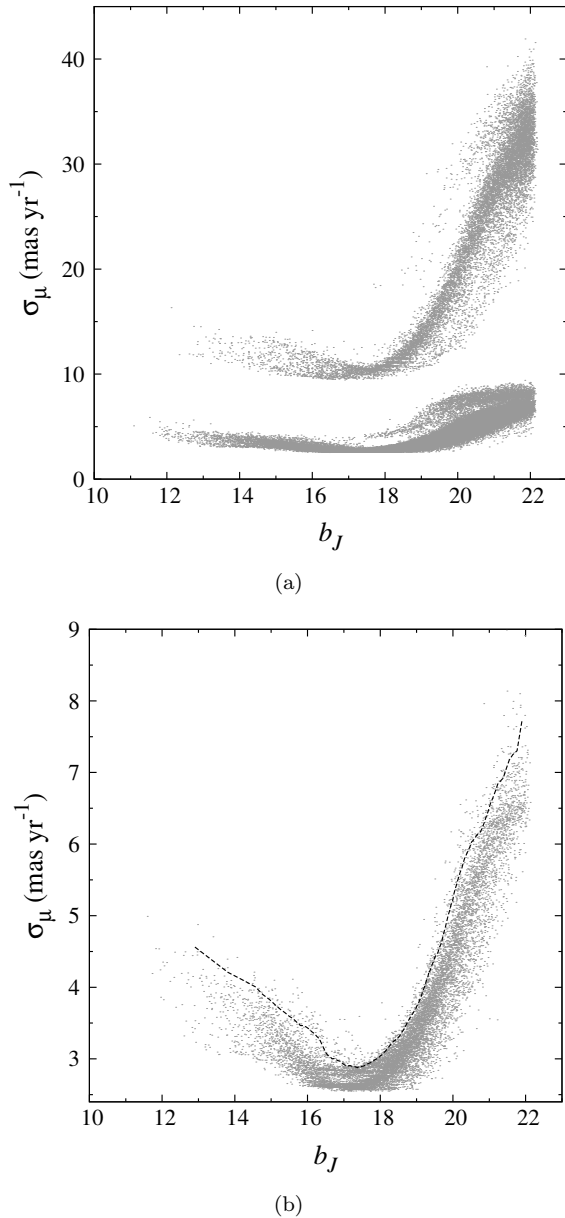


Figure 1. Field 772S proper motion errors and fitted $\sigma_\mu(b_J)$ function. (a) includes objects not detected at r_{63F} , which form the locus of points at higher σ_μ . (b) is restricted to objects with full four plate detections, and shows the function fitted to the upper boundary of the σ_μ, b_J locus.

exploiting the variable proper motion accuracy. The mean lower proper motion limit across the survey is shown in Figure 2. This is divided into the three sky regions where the source photographic data are the same. Note that the lower quality northern data attains a similar proper motion accuracy as the southern region that shares the same first epoch r material, that of the POSSI-E survey ($\delta > -18^\circ$). The ESO-R survey has a much later average epoch, with the result that proper motion measurements are considerably more uncertain.

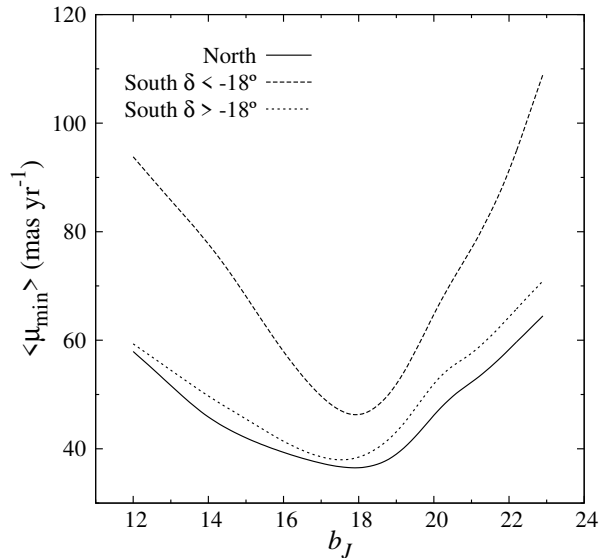


Figure 2. Mean lower proper motion limits in the three sky regions of uniform photographic source data.

2.1.2 High proper motion

The precise location of the upper proper motion limit is not as important as the lower proper motion limit from a catalogue completeness point of view, because of the low probability of finding objects at these velocities and the fact that the survey volume is not as sensitive to errors at high proper motions ($\sigma_V^2 \propto \mu^{-8} \sigma_\mu^2$). However, we expect to find a greater fraction of elusive spheroid WDs at high proper motions, and extending the range as wide as possible while limiting contamination from spurious detections allows greater constraint on the luminosity function.

With far fewer high proper motion objects present, there is insufficient statistical power to set an upper limit on a field-by-field basis and a global approach is required. We investigated the completeness of proper motions by looking at the cumulative number counts for all objects, after applying the selection cuts outlined in the remainder of this section to eliminate noise. Figure 3 shows the cumulative number counts as a function of proper motion for all survey objects, extending into the low proper motion range to demonstrate the completeness across the interface as indicated by the first vertical bar. We fix the upper limit at the point where the number counts depart from a straight line, which was judged to be at $\mu = 1''.0 \text{ yr}^{-1}$. This is marked by the second vertical bar.

2.1.3 Astrometric residuals

We place restrictions on the astrometric χ_ν^2 in order to exclude objects with a poor fit to their proper motion solution. Appropriate cuts are obtained iteratively by checking for contamination in the reduced proper motion diagram and the distribution of $\frac{V}{V_{\max}}$ for the resulting catalogue. A cut of $\chi_\nu^2 \leq 2.0$ is applied to the high proper motion data across the whole sky, and $\chi_\nu^2 \leq 1.5$ in the southern hemisphere for the low proper motion data. The low proper motion data

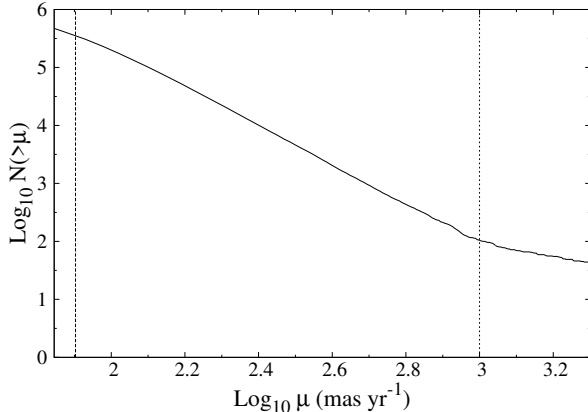


Figure 3. Completeness limit at high proper motion.

is adversely affected in the north by the lower quality plate material, and a restrictive cut of $\chi^2_\nu \leq 0.8$ is necessary.

The stars ejected from the survey by these cuts can be accounted for later by including an appropriate correction factor in the LF measurement. In both the high and low proper motion data, the requirement of a detection at all four epochs results in a four degree of freedom astrometric fit ($\nu = 4$). However, the distribution of χ^2_ν for objects in both the SSA and our high proper motion data is significantly tighter than expected. We have analyzed the astrometric residuals for objects in a selected SSS field in conjunction with synthetic data, and established that the tangent-plane position errors used in the astrometric fits are overestimated by a factor of around $\sqrt{2}$, leading to a χ^2_ν roughly half its true value. This makes the correction factor hard to determine accurately. Assuming all χ^2_ν values are halved, a $\chi^2_\nu \leq 2.0/1.5/0.8$ cut will eject around 0.5/2/20% of stars.

2.2 Magnitude limits

The SSS literature provides magnitude completeness estimates for a selection of b_J and r_{59F} plates in the first SSS data release, the South Galactic Cap (SGC). These are measured by comparing SSS star and galaxy counts with those obtained from deeper prime-focus and CCD data in overlapping regions, and estimate near 100% completeness within ~ 1.5 mags of the plate detection limits. However, our all-sky survey uses northern Schmidt plate data not included in the SGC, those of the POSS-I and POSS-II surveys. Also, the $r_{63F/103aE}$ and i_N plates are shallower and of lower signal to noise than b_J and r_{59F} , and, given the colours of the objects we are interested in, will likely determine the overall completeness limits of the SSS fields when considering objects detected on all four plates. Therefore, it is necessary to estimate new completeness limits for all plates used in the SSS. Since we cannot obtain deeper imaging for all fields, we instead follow the method of Tinney et al. (1993); this involves simulating star and galaxy counts along the line of sight, and comparing these to observed counts derived from the corresponding plate material. We assume that the completeness characteristics of plates within the same photographic survey are identical, due to uniform quality control, emulsion grade and copying history prior to digitiza-

Field	b	Ω	Surveys
411S	-86.89	0.00756	SERC- <i>J/EJ</i> SERC- <i>R</i> /AAO- <i>R</i> SERC- <i>I</i> ESO- <i>R</i>
350S	-80.18	0.00749	
241S	-69.38	0.00538	
149S	-60.60	0.00591	
237S	-50.23	0.00731	
507N	87.85	0.00759	POSSII- <i>B</i> POSSII- <i>R</i> POSSII- <i>I</i> POSSI- <i>E</i>
382N	80.98	0.00751	
270N	70.38	0.00750	
273N	59.44	0.00750	
135N	49.36	0.00723	

Table 1. Fields used to measure the completeness function for each photographic survey. b and Ω are the Galactic latitude and solid angle subtended by each field.

tion. This allows us to restrict our analysis to a representative sample of plates from each of the eight photographic surveys used in the SSS. Although the plate detection limit varies within each survey, we assume that the plates have a common *completeness function*, which we define as the ratio of detected objects to real objects as a function of magnitude relative to the plate detection limit. We analyzed five plates from each survey, drawn from five fields in each of the celestial hemispheres. A summary of the fields selected for analysis is given in Table 1.

2.2.1 Synthetic star and galaxy counts

2.2.1.1 Stars Differential star counts along the line of sight to each field are obtained using the Besançon Galaxy model (see Robin et al. 2003). This employs a population synthesis approach to produce a self-consistent model of the Galactic stellar populations, which can be ‘observed’ to obtain theoretical data sets useful for testing various Galactic structure and formation scenarios. We use the coordinates, solid angles and passbands of our selected fields as inputs, and select an output number count range that goes several magnitudes fainter than the plate limits. The SuperCOSMOS filter system is not included in the Besançon model; instead we use the CFHT Megacam bands g and r to approximate b_J and $r_{59F/63F/103aE}$, and Johnson-Cousins I to approximate i_N .

2.2.1.2 Galaxies Within a few magnitudes of the plate limits, galaxies appear as unresolved, point-like objects and have image parameters that overlap with stars. We therefore have to include galaxies in our synthetic number counts. Galaxy counts to faint magnitudes have been determined in many independent studies. We use counts provided by the Durham Cosmology Group that combine their own results (see e.g. Jones et al. 1991; Metcalfe et al. 1991) with those of many other authors. These are available online¹ along with transformations to photographic bands. They are provided in terms of log-number counts per square degree per half-magnitude; we fit straight lines to obtain functional forms for the galaxy counts in each band, and trans-

¹ See <http://astro.dur.ac.uk/nm/pubhtml/counts/counts.html>

form these to 0.1M for comparison to our observed counts. Note that the ~ 25 square degree field of view of each Schmidt plate smooths out any anisotropies in the faint galaxy counts. The fitted functions are given in Equations 1 ($r \equiv r_{59F/63F/103aE}$). The units on the number counts N are $\text{deg}^{-2} 0.1\text{M}^{-1}$. We multiply these functions by the solid angle of each field, then add them to the star counts to obtain the total synthetic counts for each plate.

$$\begin{aligned} \log(N_{b_J}) &= 0.471 b_J - 7.890 & (16 < b_J < 26) & (1) \\ \log(N_r) &= 0.379 r - 5.351 & (17 < r < 25) \\ \log(N_{i_N}) &= 0.606 i_N - 9.132 & (12 < i_N < 17.75) \\ &= 0.346 i_N - 4.397 & (17.75 < i_N < 25) \end{aligned}$$

2.2.2 Observed star and galaxy counts

For each field selected for analysis, we obtain object counts to the detection limit on all four plates, binned at 0.1 magnitude intervals server-side using an efficient SQL query on the SSA interface. We use a wide range of image statistics to include partially resolved galaxies, though close to the plate limits everything is pointlike.

2.2.3 Completeness functions and faint magnitude limits

In Figure 4 we show observed and modelled differential object counts for each plate in field 270 in the north. The ratio of these quantities relative to the detection limit gives the completeness function for the plate; these are inlaid for comparison. Total model counts are normalised to the observed number at two magnitudes above the detection limit, where the plates are assumed 100% complete. To estimate the global completeness function for each survey, we repeat the analysis for the five representative fields listed in Table 1 and take an unweighted average of the individual completeness functions. The global completeness functions obtained for the northern hemisphere surveys are shown in Figure 5 for reference. We set the magnitude limits in terms of an offset from the detection limit, defined as the magnitude of the faintest detected object. This ensures that the noise at faint magnitudes is avoided. The global completeness functions are used to judge an appropriate value. The offsets selected are listed in Table 2, along with the mean magnitude limit obtained on applying the offset to all survey plates.

The superior quality of SERC-*J* and SERC-*R* is evident, due to the use of original glass survey plates in the SuperCOSMOS scanning program. These plates show $\sim 100\%$ completeness to within a few tenths of a magnitude of the detection limit. All other surveys were copied photographically at least once before digitizing, which has resulted in noise creeping in within a magnitude or so of the detection limit. The POSSII-*I* survey was copied *twice* before scanning, and the noise is noticeably worse on these plates. The POSSI-*E* plates often show extremely large numbers of spurious detections within up to two magnitudes of the detection limit. A double peak is often seen in the distribution; this is due to the mosaicking of two or more Palomar fields of different depths onto one ESO-SERC field for inclusion in the SSS catalogue. This means that to ensure completeness, the POSSI-*E* magnitudes have to be limited to the depth of the shallowest plate in mosaicked fields, leading to the

Survey	m_{offset}	Mean mag limit
Northern hemisphere:		
POSSI- <i>E</i>	1.9	18.8
POSSII- <i>B</i>	0.4	22.2
POSSII- <i>R</i>	0.5	20.6
POSSII- <i>I</i>	0.7	18.9
Southern hemisphere:		
ESO- <i>R</i>	0.7	20.2
SERC- <i>J</i>	0.4	22.4
SERC- <i>R</i>	0.3	20.7
SERC- <i>I</i>	0.7	18.6

Table 2. Offsets defining the magnitude limit for each field in the eight constituent photographic surveys. Column three gives the average survey magnitude limit on applying these offsets globally. The number in brackets is the corresponding average when the $r_{59F} < 19.75$ constraint is applied to the second epoch r data, as explained in Section 2.2.4.

large offset of 1.9 m . This is a significant restriction on the survey volume, considering that the POSSI-*E* survey covers the whole sky down to $\delta \sim -18^\circ$.

2.2.4 Astrometric noise at faint magnitudes

Early catalogues drawn using the magnitude limits described in the preceding Section showed large amounts of contamination by faint objects with erroneous proper motions. This is most apparent in the reduced proper motion diagram that is used to select white dwarf candidates (see Section 3), where large numbers of faint disk main sequence stars with erroneous large proper motions scatter into the region populated by cool white dwarfs. Many attempts were made to restrict these objects using astrometric and image statistics, but in the end a survey-wide cut on the second epoch r_{59F} magnitude was required. We fix this cut at $r \leq 19.75$. r_{59F} is used in the primary multi-epoch object pairing, so is a good proxy for the robustness of the proper motion measurement. The numbers in parenthesis in Table 2 give the mean magnitude limit on combining this cut with the completeness limits.

This involves modelling the effective survey volume over discrete tangential velocity ranges, and turns out to be a good way to separate the disk and spheroid white dwarf populations, which are distinguishable only on the basis of kinematic study.

2.2.5 Bright magnitude limits

The selection of the bright limits on apparent magnitude is not as crucial, due to the low probability of white dwarfs being found at these magnitudes. We fix the bright limits at 12 for all bands and across all fields. This is within the complete range of the Schmidt plates.

2.3 Photometric accuracy and transmission functions

While photography cannot compete with CCD astronomy in terms of photometric accuracy, it has been noted in the

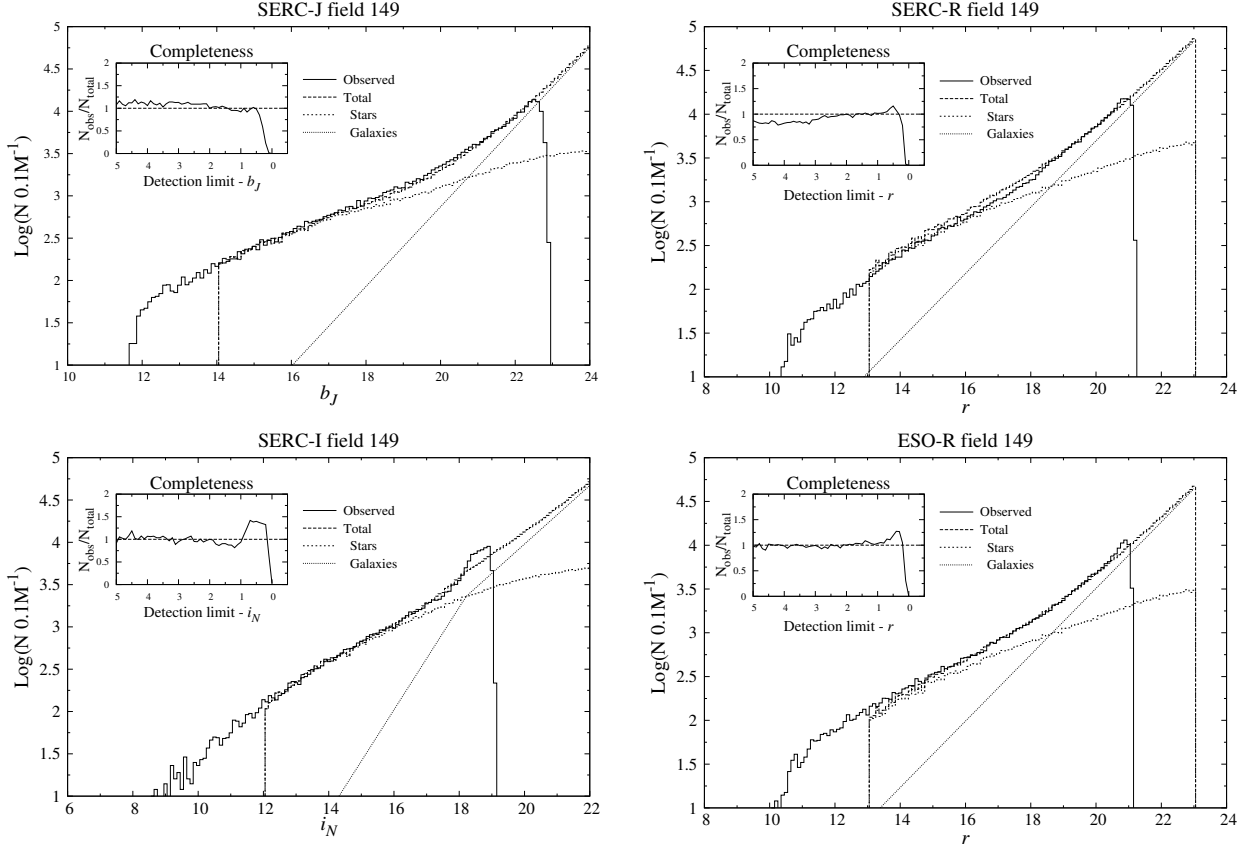


Figure 4. Example completeness analysis for two fields in the SSS, covering all eight of the constituent photographic surveys.

literature (e.g. Salim et al. 2004) that insofar as digitized photographic surveys go, SSS photometry is of the highest quality with uncertainties as low as $\sigma_m \sim 0.07$. Rough estimates of the external error on the photographic *colours* at $b_J \sim 16.5$ and $b_J \sim 20$ are given in Hambly et al. 2001b. These are used when fitting photometric models to stellar colours. We fit a straight line for the error at intermediate and fainter magnitudes, and use the uncertainty at $b_J \sim 16.5$ for all brighter magnitudes. The relation we obtain is

$$\sigma_{b-r, b-i}(b_J) = \begin{cases} 0.07 & \text{if } b_J \leq 16.5 \\ 0.026b_J - 0.35 & \text{otherwise.} \end{cases}$$

Due to the particular way in which the photometric scale is calibrated, colours are more accurate than single magnitudes. Uncertainty in single passbands is necessary however for deriving minimum-variance estimates of the photometric distance, by comparing model and observed magnitudes. These are taken from Table 12 in Hambly et al. 2001b. Filter transmission functions have been obtained from Evans (1989) (b_J) and Bessell (1986) ($r_{63F/103aE}$, r_{59F} and i_N).

2.4 Image quality criteria

Every parameterized object detection in the SSA is accompanied by a set of image statistics, some of which we restrict in order that stars included in our survey have high quality, stellar images.

Blend number We reject objects that have been de-blended at any of the four epochs. The de-blending algorithm attempts to recover individual object parameters, but is known to be unreliable.

Quality number The quality number is a 32-bit integer flag set so that increasingly significant bits indicate increasingly compromised situations encountered during image analysis. We restrict this parameter to values less than 128, which indicates an image likely to be affected by a step wedge or other label on the photographic plate.

Profile classification statistic The profile classification statistic η provides a magnitude-independent measure of the ‘stellarity’ of each image, by quantifying the deviation of the radial profile slope from that of a mean stellar template. η is given in terms of a unit Gaussian statistic, and we accept images with $|\eta| \leq 4\sigma$.

Ellipticity Previous studies utilising digitized Schmidt plate data have placed cuts on the ellipticities e of images, in order to limit contamination from faint galaxies and noise. However, we have found that the ellipticities provided by the SSA are extremely noisy at intermediate to faint magnitudes, and that any intuitively sensible cut will result in a seriously incomplete sample of stars. For example, real stellar images in the b_J band are often assigned $e > 0.5$ within

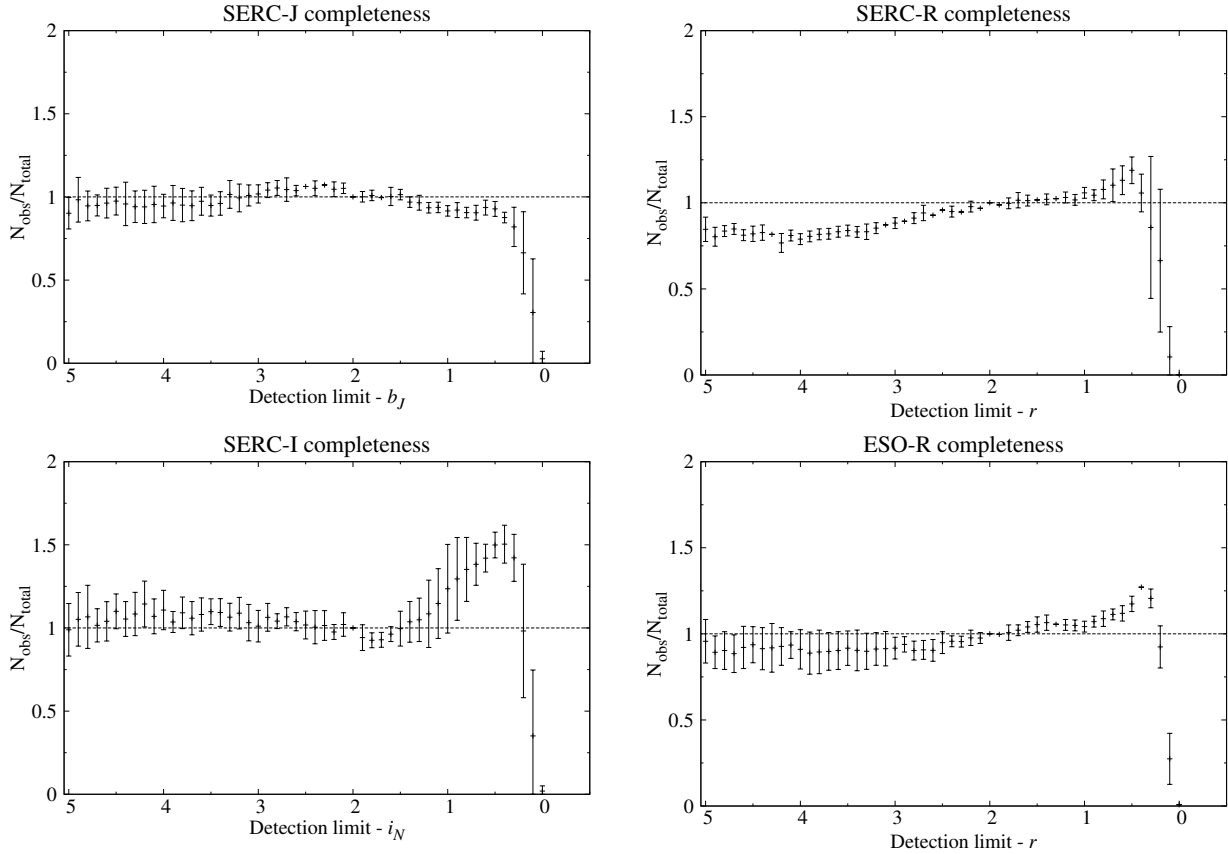


Figure 5. Completeness functions averaged over five plates in each photographic survey.

two magnitudes of the plate detection limit. We have ignored this parameter altogether.

2.5 Sky Coverage

2.5.1 Individual field areas

The pointings used for the ~ 1700 fields comprising the SSS use the ESO/SERC system of field centres, which is based on a 5° pitch angle plus some small adjustments to allow for locating guide stars. This results in $\sim 0.5^\circ$ overlap between neighbouring fields, given the $\sim 6^\circ \times 6^\circ$ field of view of Schmidt plates. Objects observed multiple times in overlap regions are assigned to the field whose centre they are closest to along a Great Circle, providing a ‘seamless’ catalogue. The coverage of each field is not given in the SSS database, and has been measured for this work. This was done numerically by dividing the sky into small elements of solid angle, accounting for any excluded regions close to the plane, and assigning each element to the field it lies closest to along a Great Circle. The average field of view for fields in the SSS is ~ 0.007 sr, with a significant spread as shown in Figure 6.

2.5.2 Bright star haloes and diffraction spikes

The fraction of each survey plate lost to internal reflections and other spurious images can be significant, and must be

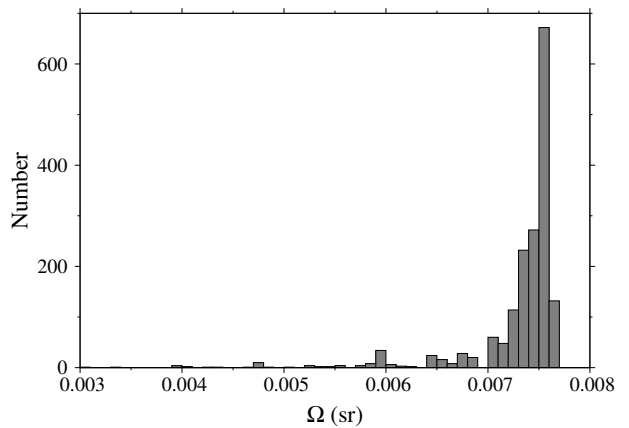


Figure 6. Frequency of non-overlapping SSS field areas.

accounted for in order to accurately calculate the survey volume. The *drilling fraction* is measured exclusively from the b_J plates, on which these images have the greatest areal extent, and ranges from a few percent at high Galactic latitude to more than 50% in the plane.

2.5.3 Rejection of crowded and dusty fields

The SSS nominally covers the entire sky. However, in dusty regions at low Galactic latitude the photometric calibration can be adversely affected by differential extinction across

Survey	$\Omega(\text{sr})$	Fraction of whole sky
$\mu < 0'18 \text{ yr}^{-1}$	9.11	0.72
$\mu > 0'18 \text{ yr}^{-1}$	8.80	0.70

Table 3. Total sky coverage of the low and high proper motion ranges.

the field. Also, in crowded regions a large amount of deblending is required, resulting in significant incompleteness as these stars are rejected by our survey procedure, and source merging across multiple epochs suffers from serious confusion. For these reasons, we avoid the Galactic plane by 10° and the Galactic centre by 20° . We also reject 53 fields lying slightly outside this region that show a large amount of contamination, manifest in highly dense regions of stars bounded by field edges. Seven fields centred on the cores of the Magellanic clouds are also excluded.

2.5.4 Rejection of fields with a small epoch spread

In most fields the earliest epoch of observation is $r_{63F/103aE}$, with the remaining three distributed over a ~ 10 to 20 year period. The primary object pairing is between the two r epochs, and if the b_J and i_N observations are taken very close to the r_{59F} observation, they provide very little astrometric constraint. In such cases, a large number of first-epoch pairings are generated for every real high proper motion object. As the search algorithm proceeds through every possible combination within the search radius, the single correct image pairing is swamped by noise. Tests show that at proper motions lower than around $0'18 \text{ yr}^{-1}$ this is not a problem, as the search radius for image pairing is small. However, at larger proper motions the effect can be catastrophic. We therefore reject objects travelling faster than $0'18 \text{ yr}^{-1}$ in any field that has b_J , r_{59F} and i_N taken within 1.5 years. 58 fields fall into this category, and are excluded. This results in slightly different sky coverage depending on the proper motion range.

2.5.5 Total sky coverage

The total survey footprint at low and high proper motions is given in Table 3. This excludes the Galactic plane and centre regions, accounts for the bright star drilling fraction, and all fields rejected from each proper motion range.

3 SURVEY SELECTION CRITERIA

3.1 Reduced proper motion selection

The proper motions of nearby stars correlate with distance, in the sense that closer objects are more likely to show large angular velocities. Proper motion can be combined with apparent magnitude to obtain a statistic called the *reduced proper motion* H , which provides a crude estimate of the absolute magnitude.

$$\begin{aligned} H_m &= m + 5 \log_{10} \mu + 5 \\ &= M + 5 \log_{10} V_T - 3.38 \end{aligned} \quad (2)$$

Population	$\langle U \rangle$	$\langle V \rangle$	$\langle W \rangle$	σ_U	σ_V	σ_W
Thin disc	-8.62	-20.04	-7.10	32.4	23.0	18.1
Thick disc	-11.0	-42.0	-12.0	50.0	56.0	34.0
Halo	-26	-199	-12	141.0	106.0	94.0

Table 4. Kinematic quantities adopted in this work. The usual Galactic coordinate axes UVW are used, with U pointing towards the Galactic centre, V in the direction of rotation, and W towards the NGP. The velocity dispersion tensor is assumed diagonal in this frame. Mean motions are relative to the Sun.

Although useless for obtaining accurate stellar distances, H is sufficient to distinguish populations of stars with distinctly different luminosity calibrations or kinematic properties. The classical tool for exploiting this is the *reduced proper motion diagram* (RPM), which plots colour against H . The RPM is topologically equivalent to the HR diagram, though with considerable vertical scatter due to the weak correlation between H and M . At around ten magnitudes fainter than main sequence stars of the same colour, white dwarfs are ideally suited to identification based on H , and several independent studies (Kilic et al. 2006, e.g.) have proved this to be a good way to compile clean white dwarf samples.

3.1.1 Tangential velocity selection

Equation 2 suggests that with an appropriate colour-magnitude relation, regions of the RPM inhabited by white dwarfs of different tangential velocity can be isolated. This allows us to perform rigorous selections on H to produce catalogues of white dwarf candidates within a well defined tangential velocity range. This is desirable because cool, low velocity white dwarfs overlap in the RPM with high velocity subdwarfs from the Galactic halo. Contamination by subdwarfs can be reduced by applying a minimum tangential velocity threshold to white dwarf candidates, producing a cleaner sample of white dwarfs by restricting selection to regions of the RPM more widely separated from the subdwarf locus. Figure 7 demonstrates the selection of white dwarf candidates based on reduced proper motion. The fact that low velocity white dwarfs are lost from the survey is of course a drawback of this technique; however, the fraction of stars that fall below the chosen threshold can be calculated, if the kinematic properties of the population are known. This is done in each field by projecting the velocity ellipsoid onto the tangent plane, correcting for the mean motion relative to the Sun, and marginalising over the position angle to obtain the distribution in tangential velocity - see Murray (1983). The values adopted for the mean reflex motions and velocity dispersion tensors are given in Table 4. These are obtained by Chiba & Beers (2000) for the thick disk and halo; for the thin disk we use the Fuchs et al. (2009) study of SDSS M dwarfs, with values taken from their 0-100pc bin that is least affected by the problems associated with the deprojection of proper motions away from the plane (McMillan & Binney 2009). Mean motions are relative to the Sun; the usual Galactic frame is used in which the velocity dispersion tensor is diagonal in σ_U^2 , σ_V^2 , σ_W^2 .

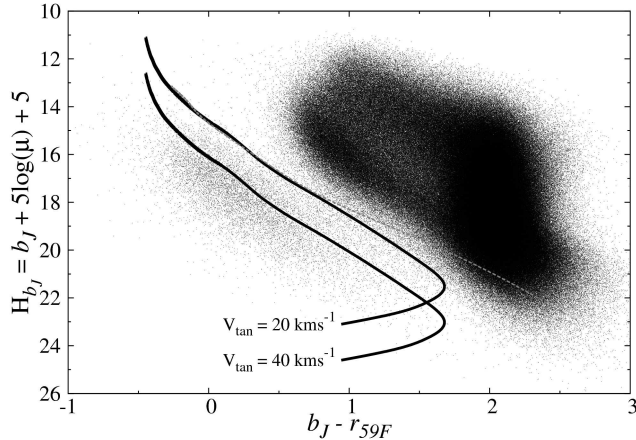


Figure 7. Reduced proper motion diagram for all stars in the SSA that pass the selection criteria described in Section 2. Overplotted are cooling tracks for H (black) atmosphere white dwarfs with $v_{tan} = 20$ and 40 km s^{-1} . Also shown is the cooling track for He (grey) atmosphere white dwarfs with $v_{tan} = 20 \text{ km s}^{-1}$. The H tracks are used to identify white dwarf candidates; all objects lying below a certain line are selected.

3.2 Photometric parallaxes

Photometric distances are obtained by fitting the two-colour photometry to the white dwarf model atmospheres and cooling sequences described in Fontaine et al. (2001) and updated in Bergeron et al. (2001) and references therein². They were provided in the SuperCOSMOS bands by Dr. Bergeron on request. The models consist of cooling sequences for white dwarfs of different surface gravity and H/He atmosphere type. The gravity and atmosphere effect the fitted distances by changing the absolute magnitude at a given colour, but with only two data points each we cannot fit these for our stars. Instead, we assume $\log g = 8.0$ for all our stars, and fit both hydrogen and helium atmospheres. It is well known that the gravities of white dwarfs are tightly distributed about this value (for example, Bergeron et al. (2001) find $\langle \log g \rangle = 8.070 \pm 0.014$), a consequence of their narrow mass distribution. Low and high mass white dwarfs exist in roughly equal numbers ($\sim 10\%$ and 15%) (Liebert et al. 2005), and fitting to $\log g = 8.0$ models has opposite effects on the photometric parallax and luminosity function.

Also, the H/He atmosphere type has very little effect on the luminosity above around $6,000 \text{ K}$ ($b_J - r_{59F} \sim 0.8$). Below this, the assumption of a H atmosphere for a He atmosphere star will cause the absolute magnitude to be considerably overestimated, and the distance underestimated. In general, optical spectra are useless for distinguishing the atmosphere type, because below around 5000 K all the absorption lines are washed out. There is therefore some ambiguity over the nature of the coolest white dwarfs in our survey.

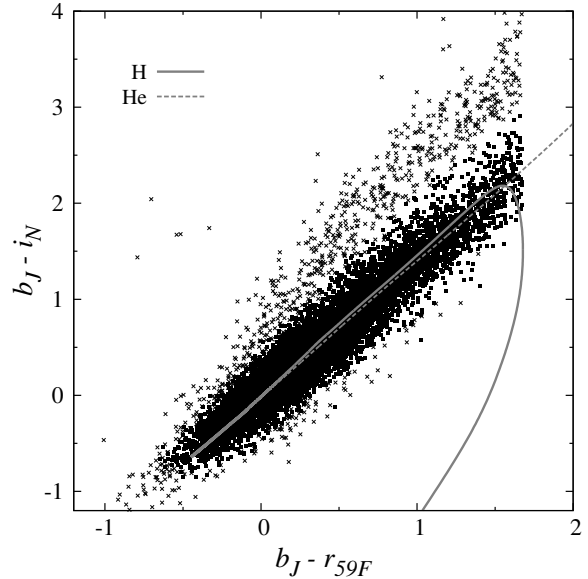


Figure 8. Two colour plot for all RPM selected WD candidates. Squares indicate stars that pass the $\chi^2 < 5.0$ cut on the model atmosphere fit; crosses indicate failures.

3.2.1 Fitting procedure

The best fitting $\log g = 8.0$ H and He atmospheres are found in a straightforward manner by variance-weighted least squares, after interpolating the models at 10 K intervals. The models corresponding to the upper and lower 1σ confidence boundaries are found by $\chi^2_{1\sigma} = \chi^2_{min} + 1$. We take no account of redenning, and do not expect it have a significant effect due to the proximity of our stars. Objects with $\chi^2_{min} > 5$ are rejected from the survey; these are mostly unresolved binaries as explained at the end of this section.

Overall distances are estimated by taking a minimum-variance combination of the estimates from each photometric band b_J , r_{59F} and i_N . Note that we avoid $r_{63F/103aE}$ in this calculation. Uncertainty on the overall distance estimate is assigned by averaging the upper and lower confidence boundaries. A two-colour diagram showing the location and status of our stars relative to the models is presented in Figure 8.

3.2.2 Calibration of photometric parallaxes

In order to estimate the accuracy of our photometric parallaxes, we compare the photometric distances to those obtained by trigonometric parallax for a subset of our white dwarfs. Bergeron et al. (2001) presented an analysis of 152 cool white dwarfs with accurate trigonometric parallaxes ($\frac{\sigma_\pi}{\pi} < 0.3$), all but two of which fall within the proper motion and magnitude range of our high proper motion data. Of the remaining 150, 116 have SSS counterparts present in our input catalogues. We investigated the missing stars by searching individual plate records for proper-motion corrected positions; mostly stars are excluded due to lack of a detection at $r_{63F/103aE}$. Note that when cross identifying stars, we do not apply the magnitude and proper motion completeness limits, as the identification is done manually and contamination is not a problem. We do, however, apply

² See www.astro.umontreal.ca/~bergeron/CoolingModels

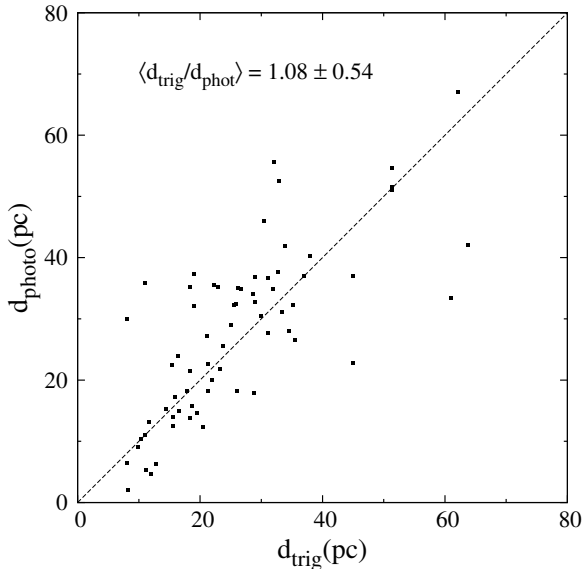


Figure 9. We compare the distances obtained by our photometric parallaxes to those obtained by trigonometric means, for a subsample of stars analysed by Bergeron et al. (2001).

the usual restrictions on blend and quality number, as these directly affect the quality of the photometry. We also require stars to be detected at all four epochs, which is necessary for the fit. These constraints reduce the sample to 75 stars.

We fit atmosphere models to the remaining stars, in each case using the appropriate H/He atmosphere as measured by Bergeron et al. (2001). We place the same cut on the residuals as is used in the main survey, in order to remove any stars with spurious photometry. This results in a sample of 68 stars with adequately fitted photometric distances. A comparison of the distances obtained by the two methods is presented in Figure 9. The correlation between the two is $r = 0.74$, and $\frac{d_{\text{trig}}}{d_{\text{phot}}} = 1.08 \pm 0.54$. The error in $\frac{d_{\text{true}}}{d_{\text{phot}}}$ is likely to be lower than this, due to uncertainty in d_{trig} , and we estimate the accuracy of our photometric parallaxes $\sigma_{d_{\text{phot}}}$ to be around 50%.

We compared the results of fitting $(b_J - r_{59F}, r_{59F} - i_N)$ and $(b_J - r_{59F}, b_J - i_N)$ colours to the models. The $(b_J - r_{59F}, r_{59F} - i_N)$ colours resulted in a slightly worse fit ($r = 0.76$, $\frac{d_{\text{trig}}}{d_{\text{photo}}} = 1.09 \pm 0.55$) presumably due to the superior quality of b_J , so we adopt $(b_J - r_{59F}, b_J - i_N)$ for performing our photometric parallax fits. We also tried relaxing the χ^2 cut to 6 then 7; in both cases the sample was increased to 70 stars with $\frac{d_{\text{trig}}}{d_{\text{photo}}} = 1.08 \pm 0.54$. Therefore, all but a few percent of white dwarfs with reliable photometry will pass the survey $\chi^2 < 5.0$ threshold.

3.2.3 Unresolved binaries

Selection of white dwarf candidates is made on b_J , r_{59F} and μ , so objects with unusual i_N magnitudes turn up at this point when their $b_J - i_N$ colours are compared to the models. The large populations of objects at red $b_J - i_N$ in Figure 8 show excess flux in i_N , due to an unresolved cool main sequence companion. These WD+dM binaries are ejected

from the survey by the restriction on the photometric parallax residuals, as with at least one of three bands polluted no reliable white dwarf fit is possible. This therefore represents a source of incompleteness in the survey. Similarly, Sirius-like systems consisting of a *hot* main sequence star and white dwarf will fail reduced proper motion selection as white dwarf candidates.

Unresolved double degenerates often have combined spectral energy distributions that closely resemble single stars of intermediate temperature. They will therefore be successfully fitted to the models and pass into the white dwarf catalogue as apparently single objects. However, with two stars contributing to the flux the derived photometric distance and tangential velocity will be underestimated by up to a factor $\sqrt{2}$.

Indications from the local (20pc) white dwarf population are that $\sim 70\%$ of white dwarfs exist as single objects (Holberg 2009). Around 20% are members of either a WD+dM or Sirius-like binary system, and so ejection of these may result in incompleteness of up to 20%, depending on what fraction are unresolved by SuperCOSMOS. Around 10% of white dwarfs exist in double degenerate binaries, which translates to a double degenerate-to-single star fraction of up to 7% among our catalogue objects, again depending on what fraction are not spatially resolved.

3.2.4 Known ultracool white dwarfs

Of the dozen or so ultracool ($T_{\text{eff}} < 4000\text{K}$) white dwarfs that have been reported in the literature, seven pass the survey constraints and are included in our white dwarf catalogue. These are LHS 3250 (Harris et al. 1999; Bergeron & Leggett 2002), CE 51 (Ruiz & Bergeron 2001), LHS 1402 (Bergeron et al. 2005), SDSSJ0947 (Gates et al. 2004), SSSJ1556 (Rowell et al. 2008), SDSSJ1452+45 and SDSSJ1632+24 (Harris et al. 2008). Our default photometric parallax method is inappropriate for these stars for two reasons. Firstly, although detailed analysis of stars of this class is currently, and necessarily, restricted to only a couple of examples, it is clear that their properties are quite different to what one would expect based on an extrapolation from higher temperatures. In particular, it would appear that most of these objects have extremely He rich atmospheres, which is difficult to reconcile with the expected accretion rates of H from the interstellar medium (Bergeron & Leggett 2002). Also, the single object with a trigonometric parallax (LHS 3250) appears over-luminous for its temperature, and has been interpreted either as an unresolved double degenerate or an extremely low mass single white dwarf. Secondly, models fail to reproduce the SEDs of these objects for *any* set of parameters, indicating incomplete input physics. To quote Harris et al. (2008), writing with reference to their own objects but applicable more generally,

“It is premature to add these new ultracool white dwarfs to any analysis of the space density and luminosity function of white dwarfs for two reasons: we do not yet have models to fit the spectra adequately to give accurate temperatures and H/He abundances, and we do not yet have distances to get luminosities, masses, and ages.”

Table 5. Distances and bolometric magnitudes for ultracool white dwarfs appearing in our survey.

Star	d (pc)	v_{tan} (kms $^{-1}$)	M_{bol}	T_{eff} (K)
CE 51	14.7 ^a	44	17.5	2730
LHS 3250	30.3 ^b	80	16.17	<4000
LHS 1402	25 ^a	58	16.8	3240
SSSJ1556	32 ^c	63	16.17	<4000
J1632+24	23 ^d	38	17.5	<3000
SDSSJ0947	47 ^e	18	16.17	<4000
J1452+45	57 ^c	28	16.17	<4000

^aPhoto π ; ^btrig π ; ^creference to LHS 3250; ^dreference to CE-51; ^ereference to LHS 3250 via SDSS colours.

While this may be true, these stars are present in our survey and must be dealt with in some way. With these caveats, we proceed to estimate distances and luminosities for these objects, though note that our adopted values should be treated with caution.

Of the seven white dwarfs, only three have anything close to a reliable distance estimate. LHS 3250 has a trigonometric parallax as noted above, and CE 51 and LHS 1402 have photometric parallaxes based on spectroscopy and multiband photometry, extending into the IR in the latter case. SSSJ1556 has a SED very similar to that of LHS 3250, and Rowell et al. (2008) invoked their similarity to assign a distance by assuming these stars also share identical luminosities. Gates et al. (2004) performed a similar analysis for SDSSJ0947 using superior Sloan photometry. We continue in this way for the final two stars. SDSSJ1452+45 is closest in colour to LHS3250, though $r_{59F} - i_N$ differs by ~ 0.4 and this star is most likely warmer. SDSSJ1632+24 has identical colours to CE 51 (to $\sim 0.01m$), and we use this star as a reference in this case. The distances and bolometric magnitudes adopted for these objects are presented in Table 5. For all objects, we adopt an identical bolometric magnitude error of $0.5M$. We have also used SSS proper motions to calculate corresponding tangential velocities. Note that on the basis of this distance estimate, SDSSJ0947 has $v_{tan} = 18\text{kms}^{-1}$ and drops out of the sample. To be clear, it passes the $v_{tan} > 20\text{kms}^{-1}$ RPM threshold for the survey, but when the extra (dubious) distance information is added at this stage it falls below the cut.

3.3 Cool white dwarf atmosphere types

At colours where the choice of atmosphere has a significant effect on the absolute magnitude, a dichotomy arises in the photometric distance estimate that must be addressed. Knox et al. (1999) deal with the unknown atmosphere type by assigning half of the stars H atmospheres and half He. However, as He WDs are brighter at a given colour they will be sampled over a larger volume and are expected to be present in greater numbers than a simple 50:50 ratio. H06 use this fact to estimate the relative numbers of the two types they expect to find in their survey, in several bolometric magnitude bins. They also avoid strict atmosphere assignments for each object, choosing instead to attach a weight to each atmosphere and allow stars to contribute as both types.

We follow the lead of H06, and assign weights to each

star depending on colour. However, instead of using a few discrete magnitude ranges, we derive a continuous weight function based on the survey volume for each each type as a function of colour. The relative fraction of He to H stars at a given $b_J - r_{59F}$ colour is estimated from the corresponding colour-magnitude relations $R_H(b_J - r_{59F})$ and $R_{He}(b_J - r_{59F})$ assuming a spherical survey volume and uniform density profile. We obtain the following formulae for the weights ω_H and ω_{He} for each type;

$$\begin{aligned}\omega_{He}(b_J - r_{59F}) &= \frac{n_{He}}{n_{He} + n_H} \\ &= \frac{1}{1 + C^{-1}10^{\frac{2}{5}(R_{He} - R_H)}} \\ \omega_H(b_J - r_{59F}) &= 1 - \omega_{He}\end{aligned}\quad (3)$$

where C is the ratio $\frac{n_{He}}{n_H}$ of He to H atmosphere white dwarfs in a fixed volume. C is likely an evolving function of colour, due to spectral evolution (see e.g. Tremblay & Bergeron 2008). Here we simply set it equal to 0.5, which is the value found by Tremblay & Bergeron (2008) for the coolest ($T_{eff} < 10,000\text{K}$) stars in their sample. This covers entirely the colour range over which the two types differ in the colour-magnitude plane, so is an appropriate assumption for all our stars. The helium weight as a function of colour is plotted in Figure 10(b) for several assumed values of C , along with reference weights obtained if H and He white dwarfs did not diverge in absolute magnitude. The diverging colour-magnitude relations used to calculate the weights are shown in Figure 10(a).

4 CATALOGUE SUMMARY

We have undertaken a proper motion and magnitude limited survey for white dwarfs in the SuperCOSMOS Sky Survey, using two distinct datasets of low and high proper motion stars. In both proper motion ranges, most WD candidates are ejected by the $r_{103aE}/63F$ magnitude limit. While this is undoubtedly the largest restriction on the catalogue size, a comparable fraction of low proper motion WD candidates are ejected by the low proper motion limits. In light of Section 3.2.2, the catalogue may be up to 50% incomplete due to exclusion of blended objects and those for which no first epoch detection exists. However, in Section 4.1 we present evidence that the incompleteness is uniform within the survey volume and does not bias the catalogue. On applying a $v_{tan} > 20\text{kms}^{-1}$ cut in reduced proper motion, we obtain 9,749 white dwarf candidates with photometric parallaxes accurate to around 50%³. Increasing the v_{tan} threshold results in a cleaner catalogue; $v_{tan} > 30\text{kms}^{-1}$ gives 8206 stars, and $v_{tan} > 40\text{kms}^{-1}$ gives 6592. Note that these numbers are based on reduced proper motion selected samples; later, we will draw velocity subsamples using the photometric parallaxes to determine velocities, and the numbers will be slightly different. A sky projection of all WD candidates that pass the $v_{tan} > 20\text{kms}^{-1}$ cut is shown in Figure 11.

³ The catalogue is available for download from <http://surveys.roe.ac.uk/ssa/links.html>

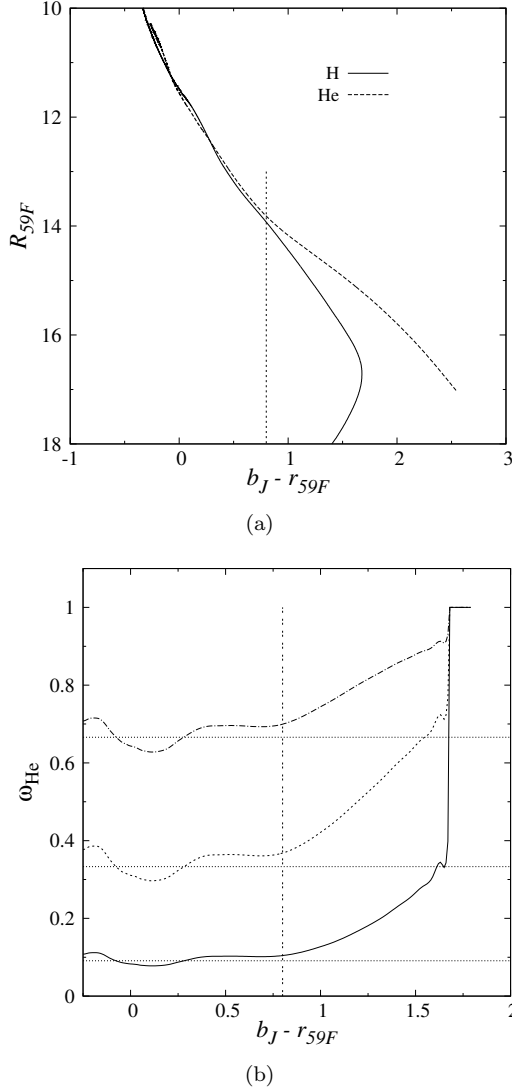


Figure 10. (a) Colour-magnitude relations for $0.6M_{\odot}$ H and He white dwarf models, showing the divergence beyond $b_J - r_{59F} \sim 0.8$. (b) Weights calculated for cool helium atmosphere white dwarfs, under different assumptions for the ratio $\frac{n_{He}}{n_H}$ in the solar neighbourhood. The curves correspond to $\mathcal{C} = 0.1, 0.5, 2.0$ (bottom to top), and the straight lines are the weights if the H and He colour-magnitude relations did not diverge.

4.1 Survey bias and incompleteness

An unbiased survey is uniformly sensitive within the accessible survey volume. The degree to which our survey meets this requirement can be checked by looking at the distribution of $\frac{V}{V_{max}}$, which follows a uniform distribution in the ideal case. V is the survey volume contained within the distance at which the star lies, and V_{max} is the maximum survey volume in which the star could reside and still be accessible to the survey. The calculation of the survey volume is non-trivial and will be explained in later Sections; here we simply present the distribution, in Figure 12. The fact the distribution is extremely flat is reassuring; this is evidence that the large incompleteness present is uniform within the survey volume, and does not bias the survey towards any particular type of star. As the stellar density profile and

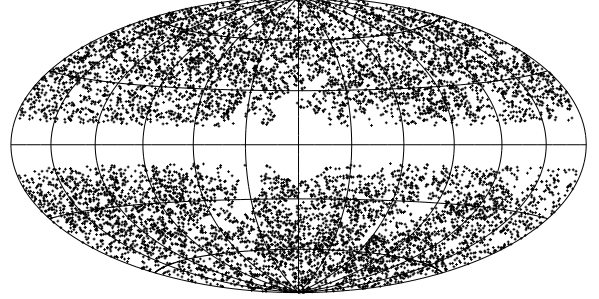


Figure 11. Hammer-Aitoff projection of WD candidates in the proper motion survey. Galactic coordinates are plotted with $l = 0$ in the centre.

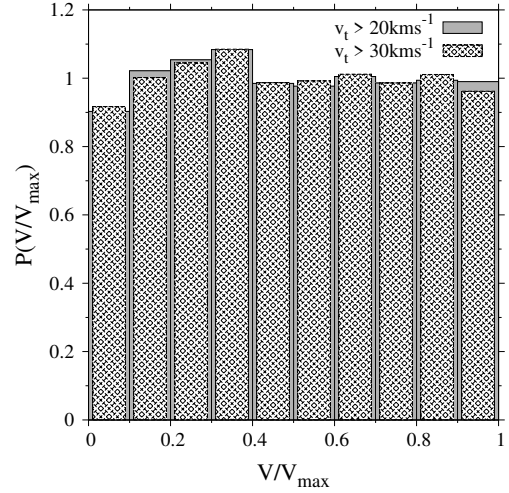


Figure 12. $\frac{V}{V_{max}}$ distribution for WD candidates with $v_{tan} > 20 \text{ km s}^{-1}$ and 30 km s^{-1} . The volume calculation assumes the density profile and velocity ellipsoid of the thin disk for all stars. $\langle \frac{V}{V_{max}} \rangle = 0.497(0.496) \pm 0.003$ for $v_{tan} > 20$ (30) km s^{-1} , with $\frac{V}{V_{max}}$ following a uniform distribution as expected. Our WD catalogue is consistent with having been drawn from an unbiased sample.

velocity ellipsoid are included in the calculation of $\frac{V}{V_{max}}$, this also suggests that reasonable values have been adopted. As $\frac{V}{V_{max}}$ is drawn from $U[0, 1]$, its distribution should have the property that $\langle \frac{V}{V_{max}} \rangle = 0.5 \pm \frac{1}{\sqrt{12N}}$ for N objects. Our $v_{tan} > 20 \text{ km s}^{-1}$ WD catalogue has $\langle \frac{V}{V_{max}} \rangle = 0.497 \pm 0.003$.

4.2 Distance and tangential velocity distributions

In Figure 13 we present the tangential velocity distribution for all objects in our WD catalogue. Clearly, a small fraction of stars show velocities much larger than those normally associated with the thin disk. Figure 14 shows the distribution of distance for all objects in our catalogue. The vast majority of stars are within 300pc, suggesting that the lack

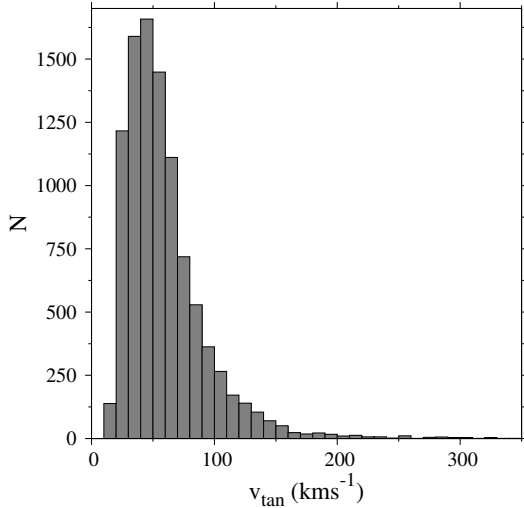


Figure 13. Tangential velocity distribution of white dwarfs in our proper motion survey.

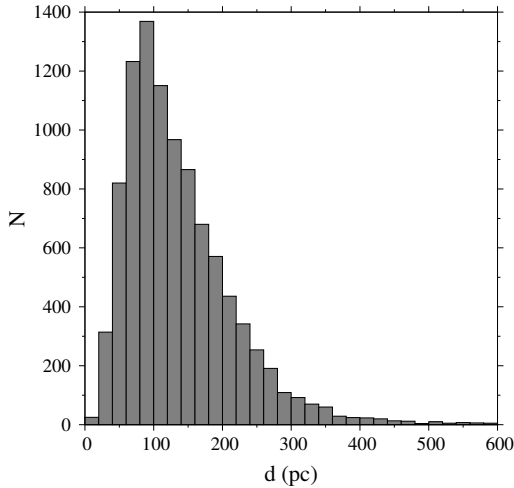


Figure 14. Distance distribution of white dwarfs in our proper motion survey.

of a reddening correction does not significantly affect the photometric parallaxes.

4.3 Comparison to H06 WD catalogue

We have compared our WD catalogue to that of H06, which was derived from a combination of SDSS DR3 and USNO-B data using much the same survey procedure as we have applied here. 1927 of our WD candidates with $v_{tan} > 30$ kms^{-1} lie in the DR3 footprint area, compared to 6009 found by H06. The difference is much larger than is accounted for by our $\sim 50\%$ incompleteness, and is a result of the wider survey limits used by H06. While our surveys reach a similar magnitude limit (they are after all based on the same photographic plate material), H06 has a much lower proper motion limit of $\mu \geq 0''.02 \text{ yr}^{-1}$. Our survey is less sensitive to proper motion but covers a much wider area, hence the comparable catalogue size overall.

Of the 1927 stars, 1135 have an unambiguous match

in the H06 catalogue. Approximately 800 of our WD candidates do not appear, presumably due to slight variations in the magnitude completeness limits between USNO-B and the SSS re-reductions of the plate material. The WD candidates that are common to both surveys show reasonable agreement on stellar parameters: photometric distances agree to 85%, and bolometric magnitudes show a dispersion of around 0.5 (assuming hydrogen atmospheres in both cases).

5 LUMINOSITY FUNCTION METHODS

5.1 The $\frac{1}{V_{max}}$ density estimator

There exists a variety of statistical methods for estimating luminosity functions, including both parametric and non-parametric methods, maximum likelihood estimators and simple number counts. The $\frac{1}{V_{max}}$ technique (Schmidt 1968) has been used in every major study of the white dwarf luminosity function, due largely to tradition and to the relative simplicity of the approach, although it has the advantage of easily incorporating proper motion selected samples, as well as the non-uniform distribution of objects within the Galactic disk. Its performance alongside other methods has been analysed by Geijo et al. (2006) and found to be satisfactory; it provides an unbiased estimate of the true density, and for large enough samples (≥ 300) accurately characterises both the rising slope and faint peak of the luminosity function.

The $\frac{1}{V_{max}}$ method obtains an estimate for the number density of objects ϕ by summing the inverse of the maximum volume in which each object could reside and still be accessible to the survey,

$$\phi = \sum_{i=1}^N \frac{1}{V_{max,i}}$$

Uncertainties are conventionally assigned assuming Poisson statistics, where the standard error in each $\frac{1}{V_{max}}$ term is equal to the term itself (e.g. 1 ± 1 events). These are then summed in quadrature to obtain the error on ϕ ,

$$\sigma_{\phi}^2 = \sum_{i=1}^N \frac{1}{V_{max,i}^2}$$

A more accurate approach would be to use the Gehrels (1986) upper and lower confidence limits for Poisson statistics, which would result in a $1^{+2.3}_{-0.83}$ contribution from each star for a 68.27% confidence interval. It is to allow comparison with other studies that we adopt an uncertainty of ± 1 on the number of stars; all previous measurements of the white dwarf luminosity function have used this.

Objects are binned on bolometric magnitude, and the density associated with each bin is calculated in this manner to obtain the luminosity function. As in Knox et al. (1999), we plot the luminosity function points at the mean magnitude of the objects in each bin. This is more realistic, and shifts the observed luminosity function slightly in regions where the number counts change rapidly with magnitude, such as at the downturn. We also assign horizontal error bars to each point, calculated by averaging the lower and

upper bolometric magnitude errors separately, e.g.

$$\sigma_{up} = \sqrt{\frac{\sum_{i=1}^N \sigma_{up,i}^2}{N}}$$

with $\sigma_{up,i}$ and $\sigma_{low,i}$ assigned from the 1σ photometric models.

5.2 Calculating V_{max}

Our survey is limited on both apparent magnitude and proper motion. The intrinsic stellar properties, namely the absolute magnitude and tangential velocity, lead to restrictions on the distance at which each star could reside and still pass the survey limits. The apparent magnitude limits are fixed in each field, and the corresponding distance limits are found according to

$$\begin{aligned} d_{max}^m &= \min \left(10^{\frac{m_{i,max} - M_i}{5}} \right) \\ d_{min}^m &= \max \left(10^{\frac{m_{i,min} - M_i}{5}} \right) \end{aligned} \quad (4)$$

where the index i iterates over each of the four bands.

Due to the non-analytic lower proper motion limits established for each field, no simple expression exists for the corresponding survey distance limits. Indeed, if the lower limit changes rapidly with apparent magnitude there may even be several ranges of distance in which the star passes the survey limits. V_{max} must be calculated by integrating the appropriate stellar density profile $\frac{\rho}{\rho_\odot}$ along the line of sight between d_{min}^m and d_{max}^m , at each step evaluating whether the star passes the proper motion limits, which are calculated from the star's apparent b_J magnitude at that distance. This leads to the integral

$$V_{max} = \sum_{f=1}^N \Omega_f \int_{r=d_{min}^m}^{d_{max}^m} \frac{\rho}{\rho_\odot} \mathcal{P}(r) r^2 . dr$$

where the summation is over all surveys fields, and

$$\mathcal{P}(r) = \begin{cases} 1 & \text{if } \mu_{min}(b_J(r)) \leq \frac{v_t}{4.74r} \leq \mu_{max} \\ 0 & \text{otherwise.} \end{cases}$$

This method for V_{max} follows that of Stobie et al. (1989), generalised to arbitrary Galactic latitudes by Tinney et al. (1993) and further here to allow for the piecewise lower proper motion limits.

5.2.1 Stellar density profiles

For the thin and thick disks we use an exponential decay law in Galactic plane distance $|z_*|$ for the stellar density profile, in order to correct for the truncation of the survey volume by the scaleheight effect. We expect to see no effect arising from the radial scalelength of the disk, due to the relative proximity of our stars. The appropriate form for $\frac{\rho}{\rho_\odot}$ is thus

$$\frac{\rho}{\rho_\odot} = \exp \frac{-|z_*|}{H}$$

where H is the scaleheight. We adopt $H = 250\text{pc}$ for the thin disk, which is in line with the result of Mendez & Guzman (1998) obtained for faint main sequence stars. These are

likely of similar age to the white dwarfs in our catalogue and are expected to show a similar spatial distribution, having been subjected to the same kinematic heating. This is also the value used in most other studies of the white dwarf luminosity function, and thus allows more meaningful comparison with other works. There is some empirical evidence that the scaleheight of disk white dwarfs increases towards fainter magnitudes (see H06) where the stars are on average older, but we ignore this here. At all but the brightest magnitudes our white dwarfs are so close to the Sun that the chosen scaleheight makes very little difference anyway.

The Solar distance from the Galactic plane, z_\odot , is often omitted in studies like this (e.g. Tinney et al. 1993), which is equivalent to setting its value to zero. However, the consensus of many star count investigations is that in fact z_\odot lies close to $\sim 20\text{pc}$ (Reed 2006). The adjusted density profile becomes:

$$\frac{\rho}{\rho_\odot} = \exp \frac{-|r \sin(b) + z_\odot|}{H}$$

where b, r are the Galactic latitude and line of sight distance and $z_\odot = 20\text{pc}$ is the Galactic plane distance of the Sun.

For the spheroid, we use a uniform density profile. We expect to see no variation in stellar density over the distances probed by our survey.

5.2.2 Corrections

Several steps in the compilation of our white dwarf catalogue have the side effect of excluding a fraction of target stars. We correct our density estimate for the ejected objects, under the assumption that the incompleteness is uniform with luminosity and does not bias the survey towards any particular type of star. The discovery fraction χ of stars that pass the tangential velocity threshold is calculated as described in Section 3.1.1, and the contribution of each star to the total density is adjusted according to

$$\phi = \sum_{i=1}^N \frac{1}{\chi_i} \frac{1}{V_{max,i}}$$

where χ for each star is taken from the field in which the star was discovered. A similar correction arises from the restriction on astrometric residuals described in Section 2.1.3.

5.2.3 Atmosphere types

Fainter than $M_{bol} = 14$ ($b_J - r_{59F} \sim 0.8$), the choice of H or He atmosphere solution has a significant effect on the fitted bolometric magnitude. In order to account for the unknown H/He atmosphere types of cool white dwarfs, stars are allowed to contribute as *both* types, with a weight set according to Equation 3. In each case, $\frac{1}{V_{max,i}}$ is simply multiplied by the appropriate weight before inclusion in the sum:

$$\phi = \sum_{i=1}^N \frac{1}{\chi_i} \left(\frac{\omega_H}{V_{max,i}^H} + \frac{\omega_{He}}{V_{max,i}^{He}} \right)$$

Note that V_{max} is different for each solution, and they will not in general contribute to the same luminosity bin. Also, the different photometric distances lead to different tangential velocities, and in some cases only one of the two solutions will pass the velocity threshold and be included in the LF.

6 THE WHITE DWARF LUMINOSITY FUNCTION

In Figure 15(a) we present the luminosity function for white dwarfs in the SSS, on adopting a 250pc scaleheight and minimum tangential velocity threshold of 30kms^{-1} . The structure in the luminosity function at the faint end is easily discernible - beyond the peak, there is a sharp drop off followed by a slow decline. Theory predicts that high mass white dwarfs cool faster than their normal mass counterparts, and, all other things being equal, fall in the region beyond the peak where the luminosity function for normal mass white dwarfs terminates. Good constraint in this region is vital for obtaining accurate age estimates, and the number of datapoints beyond the peak is encouraging. However, a quantitative analysis is only possible in conjunction with theoretical luminosity functions.

Due to the effect of the magnitude-dependent proper motion limits, at fainter bolometric magnitudes the sample is dominated by stars of brighter apparent magnitude. This improves the photometric parallax fit and reduces the width of the horizontal error bars on the luminosity function points. Beyond the peak, the sample is dominated by the ultracool white dwarfs, which have a fixed bolometric magnitude uncertainty of $0.5M$ leading to larger error bars relative to the peak.

Figure 15(b) shows the effect on the luminosity function when the lower tangential velocity threshold is varied. The fact that no systematic trends are apparent in the luminosity function suggests that the sample is not significantly contaminated by subdwarfs at low velocities.

6.1 The luminosity function for high velocity white dwarfs

Any spheroid white dwarfs present in our catalogue may be identified by their large tangential velocities. Figure 16 shows the tangential velocity distributions for the thin disk, thick disk and spheroid along the line of sight to one of our survey fields, as determined from M dwarfs and low metallicity stars (see Fuchs et al. 2009; Chiba & Beers 2000). A cut of $v_t > 200\text{kms}^{-1}$ is often considered to cleanly separate the spheroid and disk populations, and the luminosity function obtained on applying this cut to our catalogue is presented in Figure 17(a). In this case, the discovery fractions used to correct for the excluded low velocity stars are calculated from the spheroid velocity ellipsoid, and the density profile is that of a uniform population. The effect of varying the velocity threshold is investigated in Figure 17(b). The fact that the $v_t > 160\text{kms}^{-1}$ luminosity function sits at a slightly higher density suggests that there is some residual contamination from the disk even at these velocities.

The origin of the high velocity white dwarf component can be further probed by looking at the bulk motion. Attributing individual stars to a particular kinematic population based on tangential velocity alone is tricky, because the kinematic properties of cool white dwarfs are relatively uncertain, and it is possible that the high velocity tail of the disk population(s) overlaps considerably with the spheroid (see Reid 2005). Ideally, radial velocities would complete the full 3D space motion in Galactic coordinates, allowing far better discrimination for individual stars. However,

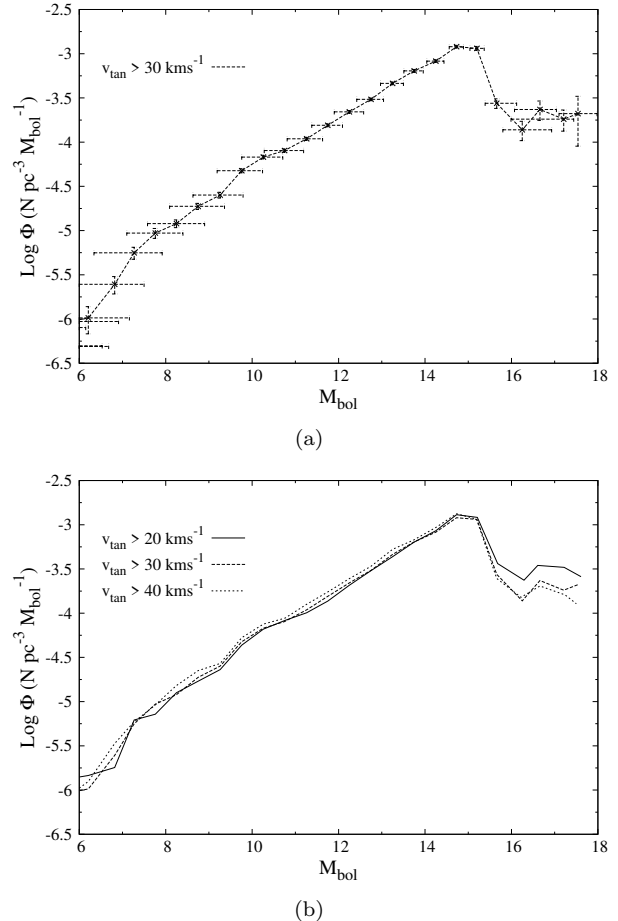


Figure 15. (a) Luminosity function for $v_t > 30\text{kms}^{-1}$ white dwarfs in the SSS. (b) Luminosity functions for white dwarfs on adopting a range of lower tangential velocity cuts.

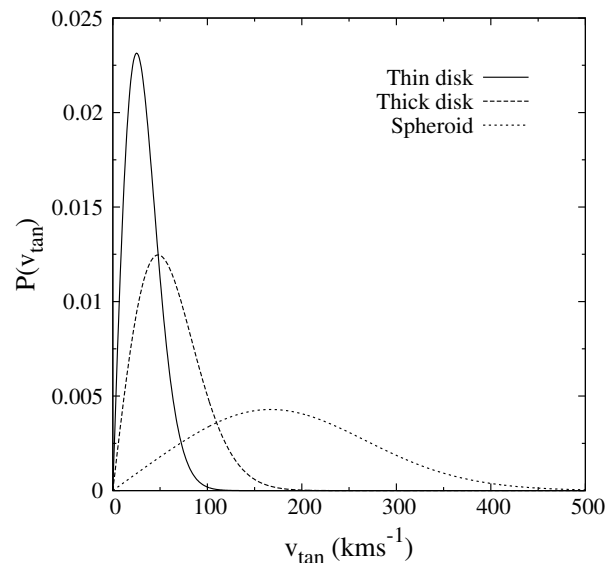


Figure 16. Tangential velocity distributions for the three major kinematic populations, along the line of sight to field 362 in the southern hemisphere. A cut of $v_t > 200\text{kms}^{-1}$ is often considered to cleanly separate the spheroid and disk populations.

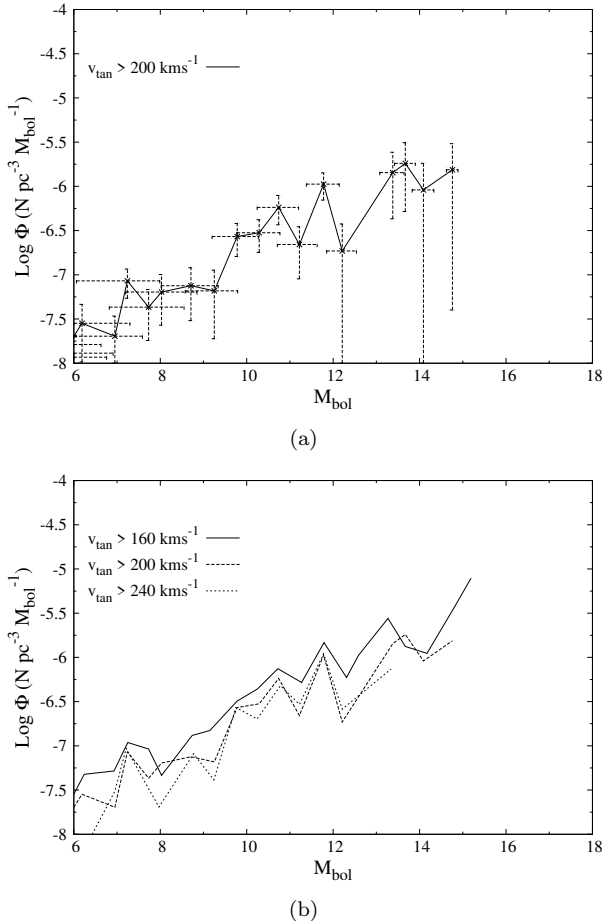


Figure 17. Luminosity functions for high tangential velocity white dwarfs. Figure (a) shows the LF for $v_t > 200 \text{ km s}^{-1}$ WDs, and figure (b) compares the LFs obtained when the lower velocity limit is varied.

with only proper motions it is still possible to measure the *mean* motion in Galactic coordinates for the population as a whole, which is sufficient to distinguish a spheroid sample from one drawn from a rotating disk. This is done by deprojecting the proper motions, according to the method used by Dehnen & Binney (1998) to analyse the kinematics of stars in the Hipparcos catalogue.

On doing so, we find that the 93 stars with $v_t > 200 \text{ km s}^{-1}$ have $\langle UVW \rangle = (-88 \pm 12, -214 \pm 24, -38 \pm 5) \text{ km s}^{-1}$. These would suggest that the high velocity members of our WD catalogue samples are drawn from a non-rotating population, i.e. that of the spheroid. We therefore conclude that the luminosity function presented in Figure 17(a) is representative of the spheroid white dwarf population.

6.2 Local disk and spheroid white dwarf densities

Integrating the luminosity function presented in Figure 15(a) gives a total local density for white dwarfs in the solar neighbourhood of $(3.19 \pm 0.09) \times 10^{-3} \text{ pc}^{-3}$

The spheroid white dwarf luminosity function of Figure 17(a) integrates out to $(4.4 \pm 1.3) \times 10^{-6} \text{ pc}^{-3}$, resulting in a disk-to-spheroid ratio of 725 ± 215 disk stars to every spheroid star. These densities are significantly lower than

those obtained by other studies, e.g. H06 find $4.6 \times 10^{-3} \text{ pc}^{-3}$ and Leggett et al. (1998) find $3.4 \times 10^{-3} \text{ pc}^{-3}$ for the local density of disk white dwarfs, and H06 find $4 \times 10^{-5} \text{ pc}^{-3}$ for those of the spheroid. If we recall from Sections 3.2.2 and 4.1, our catalogues may be up to 50% incomplete due to blended objects and those missed at first epoch r , which explains the disagreement between these numbers. This incompleteness is expected to be uniform with bolometric magnitude, and therefore will not affect the disk-to-spheroid ratio, nor will it affect any conclusions about the age of these two populations, as this is insensitive to the normalisation of the luminosity function. It should be noted at this point that while the disk WDLF almost certainly falls rapidly to zero beyond the magnitude range of our survey, the spheroid WDLF most likely continues rising to fainter magnitudes. Deeper surveys may find significantly larger integrated densities for the spheroid by including fainter magnitude bins, and the numbers presented here should be regarded as lower limits. The contribution from fainter objects may also be constrained using theoretical luminosity functions, however we do not do this here.

7 UNTANGLING THE DISKS AND SPHEROID

The technique of drawing velocity selected sub-samples of stars works reasonably well at isolating a clean sample of spheroid stars. Although uncontaminated by disk stars, samples drawn in this manner do of course miss a large fraction of spheroid stars at lower velocities, where they are indistinguishable from the disk. Also, the thin and thick disks could never be separated in this manner, due to the large overlap in tangential velocity leaving no range in which the populations can be reliably isolated from each other or the spheroid. It is worth pointing out that chemical tagging, as might be used to distinguish the main sequence members of these populations, cannot be used for white dwarfs as any photospheric metals sink rapidly below the photosphere.

An alternative approach can be derived by considering the how the sampled volume for each of the kinematic populations affects the numbers of stars that make their way into the survey. The total number of survey stars, N_* , is determined by the local number density n multiplied by the survey volume V , separately for each kinematic population,

$$N_* = n_{\text{thin}} \times V_{\text{thin}} + n_{\text{thick}} \times V_{\text{thick}} + n_{\text{sph.}} \times V_{\text{sph.}} \quad (5)$$

where the subscripts refer to each of the major kinematic populations. In a narrow range of magnitude, such as one of our luminosity function bins, the factor that determines V for each of the populations is the tangential velocity distribution combined with the survey proper motion and tangential velocity limits. The magnitude limits are effectively decoupled from the analysis, because stars belonging to each population have very similar mean absolute magnitudes over the small ranges considered. The kinematics differ considerably however, and for equal survey limits each population will be sampled over a different volume of space. By varying the tangential velocity limit, and recalculating each V for the new N_* , a set of linear equations in the unknowns densities n can be generated. In general, the equation set is non-singular and solvable using linear algebra techniques.

The power of this approach lies in the fact that individual stars are not assigned conclusively to either population. Instead, it simply measures the fraction of stars that belong to each population, as a function of v_t . Note that we will refer to the survey volume measured in this technique as the *effective volume*, V_{eff} , to distinguish it from that used in the conventional $\frac{1}{V_{\text{max}}}$ technique. In this approach no strict distance boundaries arise from the proper motion limits and the survey is sensitive to some velocity sub-sample at all distances.

7.1 Modelling the effective volume

The survey volumes used in this analysis are calculated in a rather different manner to V_{max} from Section 5.2. This is because neither the absolute magnitude nor tangential velocity are directly observed from the survey objects. In the first instance, we instead use the theoretical mean absolute magnitude for all stars in each luminosity bin, obtained by integrating model $M(M_{\text{bol}})$ relations for each survey band. We assume the LF is flat over the width of each bin, and use standard $\log g = 8.0$ DA models; the difference between the effective volumes for DA and DB models is very small at fixed bolometric magnitude. These are then used in conjunction with the apparent magnitude limits in each survey field to place limits on the distance at which this hypothetical star could lie and still pass the magnitude limits. These are found according to

$$\begin{aligned} d_{\text{max}}^m &= \min \left(10^{\frac{m_{i,\text{max}} - \langle M_i \rangle}{5}} \right) \\ d_{\text{min}}^m &= \max \left(10^{\frac{m_{i,\text{min}} - \langle M_i \rangle}{5}} \right) \end{aligned} \quad = \quad \begin{bmatrix} N_*(\delta v_1) \\ N_*(\delta v_2) \\ N_*(\delta v_3) \\ \vdots \\ N_*(\delta v_m) \end{bmatrix}$$

which is similar to the expression in Equation 4 except the observed absolute magnitude has been replaced by the theoretical mean for the LF bin.

The effective survey volume for each kinematic population is then found by integrating the appropriate density profile $\frac{\rho}{\rho_{\odot}}$ between d_{min}^m and d_{max}^m , at each step correcting for the fraction of stars that pass the tangential velocity limits at that distance. The survey volume is thus marginalised over the tangential velocity, leading to the effective volume probed for each population. This is done as follows,

$$V_{\text{eff}} = \sum_{f=1}^N \Omega \int_{r=d_{\text{min}}^m}^{d_{\text{max}}^m} \frac{\rho}{\rho_{\odot}} r^2 \chi(r) dr$$

where the summation is over all survey fields. The factor $\chi(r)$ is the discovery fraction of stars that pass the tangential velocity limits at distance r , and is calculated from the cumulative distribution by

$$\chi(r) = \text{cdf}((v_{\text{upper}}(r)) - \text{cdf}((v_{\text{lower}}(r)))$$

where v_{upper} and v_{lower} are tangential velocity limits fixed by the survey design. The appropriate v_{upper} and v_{lower} are found according to

$$\begin{aligned} v_{\text{upper}}(r) &= \min(v_{\text{max}}, 4.74 \mu_{\text{max}} r) \\ v_{\text{lower}}(r) &= \max(v_{\text{min}}, 4.74 \mu_{\text{min}} r) \end{aligned}$$

where v_{max} and v_{min} are external tangential velocity limits that may be applied to restrict the velocity range, and the

second argument in each case is the velocity limit arising from the survey proper motion limits at distance r .

The velocity ellipsoids adopted are those of Table 4. As before, a uniform density profile is used for the spheroid and a 250pc scaleheight exponential disk is used for the thin disk. The thick disk density profile is that of a 1500pc scaleheight exponential disk; however, the proximity of our stars means the effective volume is rather insensitive to the scaleheight at this level, and it is the velocity correction alone that separates the thick disk and spheroid populations in our survey.

7.2 Solution for the number density

Applying external v_{min} and v_{max} cuts enables one to generate several instances of Equation 5, which can be used to construct a linear equation set in the unknown densities. We use non-overlapping v_{tan} ranges to construct each equation, so that the covariance of neighbouring star count bins is zero. The set of equations can be cast in matrix form like

$$\begin{bmatrix} V_{\text{thin}}(\delta v_1) & V_{\text{thick}}(\delta v_1) & V_{\text{sph.}}(\delta v_1) \\ V_{\text{thin}}(\delta v_2) & V_{\text{thick}}(\delta v_2) & V_{\text{sph.}}(\delta v_2) \\ V_{\text{thin}}(\delta v_3) & V_{\text{thick}}(\delta v_3) & V_{\text{sph.}}(\delta v_3) \\ \vdots & \vdots & \vdots \\ V_{\text{thin}}(\delta v_m) & V_{\text{thick}}(\delta v_m) & V_{\text{sph.}}(\delta v_m) \end{bmatrix} \begin{bmatrix} n_{\text{thin}} \\ n_{\text{thick}} \\ n_{\text{sph.}} \end{bmatrix} = \begin{bmatrix} N_*(\delta v_1) \\ N_*(\delta v_2) \\ N_*(\delta v_3) \\ \vdots \\ N_*(\delta v_m) \end{bmatrix}$$

where $\delta v_{1,2,\dots,m}$ are the chosen tangential velocity ranges. Investigations indicate that a suitable set of velocity ranges is $30 < v_1 < 50 \text{ km s}^{-1}$, $50 < v_2 < 80 \text{ km s}^{-1}$, $80 < v_3 < 120 \text{ km s}^{-1}$, $120 < v_4 < 200 \text{ km s}^{-1}$ and $200 < v_5 < \infty \text{ km s}^{-1}$, thus sampling at finer resolution at highly populated velocities where the relative contributions of each population change rapidly, and probing the region of pure spheroid stars at the extreme. In short hand,

$$V \mathbf{n} = \mathbf{N}$$

We assume no errors on the design matrix V , permitting a reasonable solution to be obtained by weighted least squares. The weighted least squares solution for \mathbf{n} , denoted $\hat{\mathbf{n}}$, is given by

$$\hat{\mathbf{n}} = (V^{\dagger} W V)^{-1} (V^{\dagger} W \mathbf{N})$$

where † denotes the matrix transpose. We use a non-negative least squares algorithm to enforce the positivity constraint on the parameters (Lawson & Hanson 1974). W is the matrix of weights, which we set according to

$$W = \begin{bmatrix} \frac{1}{\sigma_{N_1}^2} & 0 & 0 & \cdots & 0 \\ 0 & \frac{1}{\sigma_{N_2}^2} & 0 & & \\ 0 & 0 & \frac{1}{\sigma_{N_3}^2} & & \\ \vdots & & & \ddots & \\ 0 & & & & \frac{1}{\sigma_{N_m}^2} \end{bmatrix}$$

i.e. inverse variance weights, adopting Poisson statistics to estimate the noise on the observed number counts. For discrete tangential velocity ranges, there is no covariance between adjacent number count bins and the weight matrix is diagonal. The uncertainties on \hat{n} are obtained from the variance-covariance matrix \mathcal{V} calculated

$$\mathcal{V} = (V^\dagger W V)^{-1}$$

and we adopt these as the formal uncertainties on the LF points. Note that the use of theoretical mean absolute magnitudes removes the horizontal error bars.

7.3 The luminosity functions for the disks and spheroid

The luminosity functions for the thin disk, thick disk and spheroid obtained on applying this technique to our white dwarf catalogue are presented in Figure 18. Note that we do not connect up luminosity function points across empty magnitude bins, where no solution was found for one or more of the populations. The turnover in the thin disk is apparent at around $M_{bol} = 15.75$, in agreement with other works. In contrast, the spheroid luminosity function continues to rise to the faintest detected magnitudes. No solution is found for the spheroid in a single bright magnitude bin at $M_{bol} = 12.75$, which is most likely due to statistical fluctuations in the spheroid number counts rather than a failure of the model.

The thick disk emerges nicely as an intermediate density population between the thin and thick disks. There is some indication of a turnover at faint magnitudes, but again the constraint is too poor to draw firm conclusions and beyond $M_{bol} = 15.25$ this population is lost altogether. The fact the thin and thick disks reach approximately equal density at magnitudes brighter than $M_{bol} \sim 7$ is interesting, and may hold information about the relative star formation histories of these populations. However, the χ^2_ν statistic presented in the lower right tile indicates that a two component model excluding the thick disk would fit the data only marginally worse than the three component model at these magnitudes, so the detection of the thick disk as a distinct entity is not conclusive. It may be the case that the scaleheight or velocity ellipsoid of the thick disk white dwarfs is closer to that of the thin disk at these magnitudes.

We applied this technique to our white dwarf catalogue several times using different combinations of the kinematic populations, to check that the model required all three populations to fit the data. The presence of the spheroid stars can be proved by conventional techniques (c.f. Section 6.1), but the thick disk can only be detected by looking for a significant improvement in the fit when it is included in the model. The upper χ^2_ν plot indicates that models with just a thin disk, or with a thin disk and spheroid, fit the data very poorly. In the lower panel we have included the thick disk; the fit is clearly much better, so we regard this as the first detection of the thick disk white dwarf luminosity function. The fit is improved marginally by the inclusion of the spheroid population.

The faintest few bins are very poorly constrained, and are significantly more uncertain than the constraint achieved using the traditional $\frac{1}{V_{max}}$ method. This is disappointing because good constraint at these magnitudes is necessary for

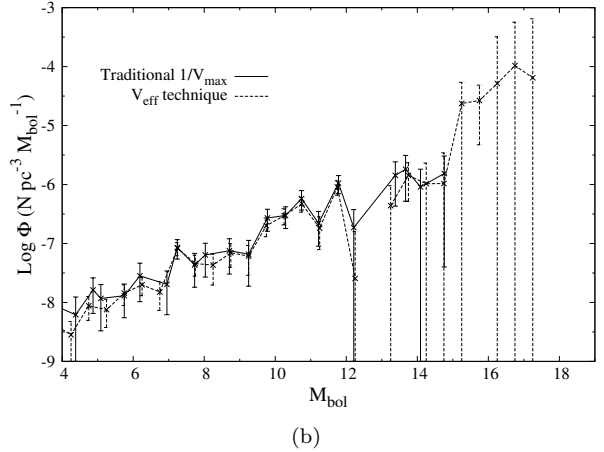
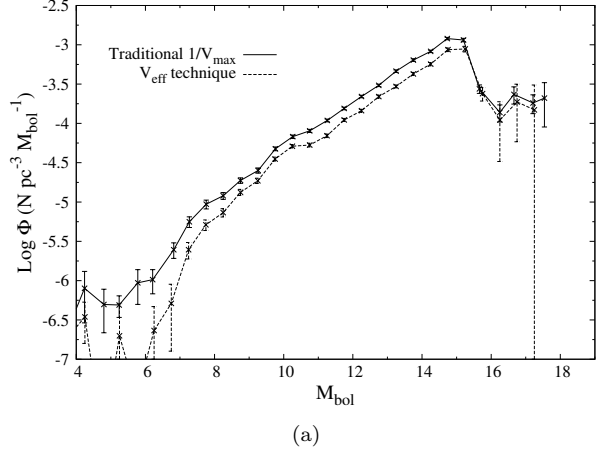


Figure 19. Comparison between LFs obtained by traditional $\frac{1}{V_{max}}$ and our effective volume technique. In the case of the thin disk (19(a)), the lower density found by the effective volume technique is due to the fact thick disk objects have been excluded. Both techniques agree well on the spheroid luminosity function because a clean sample can be isolated for the $\frac{1}{V_{max}}$ method. However, the effective volume technique has a smaller error because the spheroid stars at low velocity are included in the solution.

accurate age measurement. Most of the age information is contained in the depth and position of the turnover at faint magnitudes, although quantitative conclusions require analysis in conjunction with theoretical luminosity functions. The three component model also fails at these magnitudes as no positive solution is found for the thick disk. This means the densities recovered for the thin disk and spheroid are somewhat compromised. The reason for this may be due to the fact the faint bins are dominated by the ultracool white dwarfs, which have particularly uncertain photometric parallaxes and bolometric magnitudes. It may also be the case that the both the velocity ellipsoid and scaleheight of the faintest disk white dwarfs are inflated relative to brighter stars, due to the faint stars being on average older. This would result in incorrect effective volumes and an inappropriate model. In Figure 19, we compare the thin disk and spheroid luminosity function obtained using the effective volume approach to those obtained from the same star catalogue using the conventional $\frac{1}{V_{max}}$ technique. In the case of

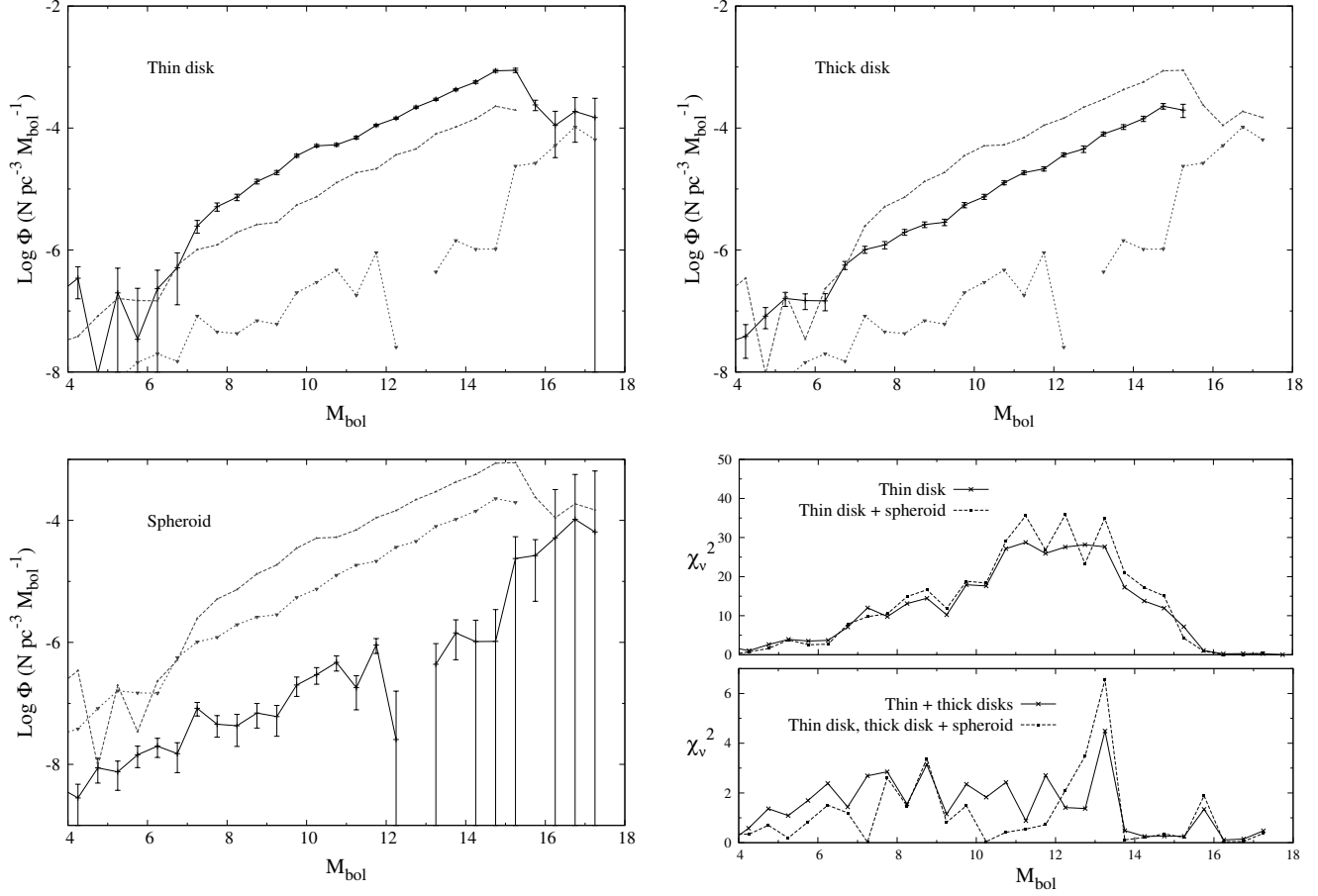


Figure 18. The luminosity functions for thin disk, thick disk and spheroid white dwarfs, obtained from our catalogue using the effective volume method. The lower right tile shows the χ^2 statistic for each luminosity bin, using different models to predict the observed star counts.

the thin disk (19(a)), the lower density found by the effective volume technique is due to the fact thick disk objects have been excluded. The traditional $\frac{1}{V_{max}}$ technique used in previous studies of the disk white dwarf luminosity function does not distinguish thin and thick disk stars, so in this case and all others the ‘thin disk’ luminosity function is really a sum of both the thin and thick disks. Both techniques agree well on the spheroid luminosity function, because a clean sample can be isolated for the $\frac{1}{V_{max}}$ method. However, the effective volume technique has smaller error bars on all points because the spheroid stars at low velocity are included in the solution. It is also able to probe 2.5 magnitudes deeper, although only one of these bins has reasonable constraint on the density.

7.4 Thin disk/thick disk/spheroid normalisation

Integrating the luminosity functions in Figure 18 allows us to measure the total and relative densities of the different kinematic populations in the Solar neighbourhood. For the thin disk, we find a total density of $(2.23 \pm 0.17) \times 10^{-3} \text{pc}^{-3}$. This is somewhat smaller than that measured in Section 6.2,

due to the exclusion of thick disk objects here⁴. For the thick disk, we find a total density of $(4.55 \pm 0.41) \times 10^{-4} \text{pc}^{-3}$, and for the spheroid we find $(1.4 \pm 5.6) \times 10^{-4} \text{pc}^{-3}$. The spheroid density is considerably larger than that of Section 6.2 due to the fact the luminosity function extends to much fainter magnitudes where the density is greater. However the same caveat applies; the spheroid WDLF may extend to considerably fainter magnitudes than probed here, so the density should be regarded as a lower limit.

We can correct these values for the incompleteness in our survey if we assume the difference between the disk density measured in Section 6.2 and that measured by H06 is due to the incompleteness. This boosts the densities to $3.1 \times 10^{-3} \text{pc}^{-3}$, $6.4 \times 10^{-4} \text{pc}^{-3}$ and $1.9 \times 10^{-4} \text{pc}^{-3}$ for the thin disk/thick disk/spheroid. Using these numbers, the total local density of white dwarfs is split among the kinematic populations in roughly 79%/16%/5%. This agrees well with predictions based on Galactic models, in particular the results of Reid (2005) who adopts numbers similar to these to successfully reproduce the results of a number of proper motion surveys for white dwarfs. The similarity between Reid’s

⁴ Note that the thick disk density is not equal to the difference, because in Section 6.2 the V_{max} for each thick disk object is calculated using the thin disk density profile and velocity ellipsoid.

Figure 9 and our luminosity functions in Figure 18 is striking.

8 COMPARISON TO OTHER WORKS

The most directly comparable white dwarf luminosity function to this study, in terms of number of stars and survey technique, is that of H06. These authors used proper motions derived from a combination of SDSS and USNO-B astrometry to obtain a sample of 6000 white dwarfs with $v_t > 30 \text{ km s}^{-1}$, with photometric parallaxes obtained from superior 5 band SDSS photometry. Their disk luminosity function is shown in Figure 20(a), alongside our own reproduced from Figure 18. At the bright end, the luminosity function of Krzesinski et al. (2009) is shown, also obtained from the SDSS but using selection based on UV excess to assemble a sample of hot white dwarfs. The most obvious difference in the thin disk luminosity functions (top panel) is the rather large vertical offset, which is due to a combination of the incompleteness in our survey, and the fact that our luminosity function is exclusively for thin disk objects whereas those shown for comparison contain thick disk objects as well. At the bright end the luminosity functions diverge, with ours finding a considerably lower density for hot white dwarfs. Our luminosity function obtained using the $\frac{1}{V_{max}}$ method agrees much better (e.g. Figure 19(a)), so the difference may be due to a genuine change in the relative contributions of the thin and thick disks at these luminosities. However, Section 7.3 suggests the thin and thick disk decomposition may be unreliable in this range. There are some striking similarities between these luminosity functions too. In particular, they agree very well on the position of the turn over at the faint end, a feature arising from the finite age of the Galaxy. Our $\frac{1}{V_{max}}$ luminosity function finds the same result, while achieving greater constraint. The inflexion at $M_{bol} \sim 11$ identified by H06 seems to be confirmed by this study. This feature may hold valuable information about the recent star formation history of the disk.

The spheroid luminosity functions (lower panel) show the same vertical offset, though this is less significant due to the larger errors. Morphological features of note include the slope of the luminosity function at brighter magnitudes where the constraint is good, and the rather more uncertain upturn at around $M_{bol} \sim 15$. Both surveys seem to agree on these features. Our spheroid luminosity function has considerably smaller error bars at magnitudes where the surveys overlap, and probes two and a half magnitudes fainter.

9 CONCLUSIONS

9.1 Proper motion survey and the luminosity function for white dwarfs

We have conducted a wide-angle survey for white dwarfs using data from the SuperCOSMOS Sky Survey and reduced proper motion selection. Our catalogue contains 9749 WD candidates on applying a $v_{tan} > 20 \text{ km s}^{-1}$ threshold, with photometric distances accurate to around 50%. Our catalogue suffers from $\sim 50\%$ incompleteness due to the ejection of blended objects and those undetected at the first epoch, however this has been shown to be uniform and does not

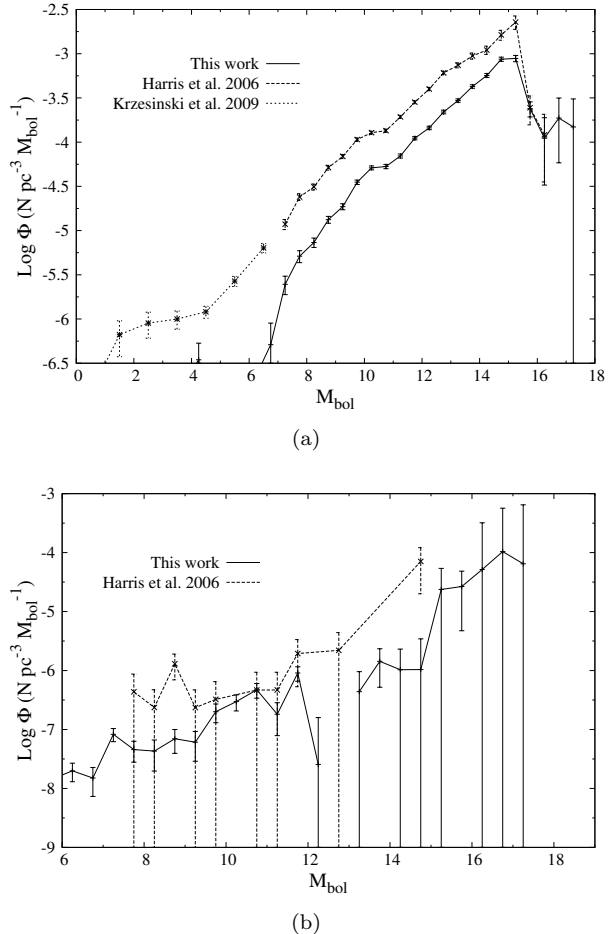


Figure 20. Figure (a) compares the decomposed thin disk luminosity function derived in this work with that of H06 and Krzesinski et al. (2009) who use traditional methods. The vertical offset is a combination of uniform incompleteness and the ejection of thick disk objects from our luminosity function. Figure (b) shows the H06 luminosity function for white dwarfs with $v_t > 200 \text{ km s}^{-1}$, as well as our decomposed spheroid luminosity function.

bias the survey. Although the normalisation of the resulting luminosity functions is compromised their morphology is not, and any cosmochronology measurements using luminosity function models will likewise be unaffected.

We have introduced a new technique to decompose a single mixed catalogue of stars into the contributions from each kinematic component, and used this to measure the thin disk, thick disk and spheroid WDLFs separately. This is the first direct measurement of the thick disk WDLF. Our thin disk and spheroid WDLFs probe 1.0 and 2.5 magnitudes deeper than the next deepest study (H06). By integrating the WDLFs we have measured the relative contributions to the total WD density in the Solar neighbourhood from each of the kinematic populations, finding results in good agreement with predictions.

The excellent agreement between our thin disk WDLF and that of H06 confirms the location of the faint turnover at $M_{bol} = 15.75$. This is surely now a secure result. An interesting feature in the rising slope of the thin disk WDLF that is also observed by H06 would seem to be confirmed by

our results. At $M_{bol} \sim 11$ WD cooling times are of the order 500 Myr, so this feature may arise from recent star formation activity in the disk.

9.2 Decomposing the kinematic populations in the Solar neighbourhood

Our work presents a useful way to decompose the otherwise indistinguishable WD components of the Galactic kinematic populations in the Solar neighbourhood, although our survey does not probe faint enough magnitudes to reach the WDLF terminus in each case. This technique may be applied to other types of star, although it is of particular application in WD studies due to the fact that metallicity cannot be used to assign population membership, and the lack of spectral lines in cool stars means radial velocities are not available.

As our method separates the populations based on their tangential velocity distributions, the fact that there has been no rigorous study of the kinematics of faint white dwarfs means our velocity dispersions (adopted from main sequence stars) must be considered a source of error. For example, assuming a thin disk velocity ellipsoid that is narrower than the true value may result in the thick disk being over populated in our models. It may also be the case that WDs at the faint end of the thin disk luminosity function have undergone significantly more kinematic heating than those at brighter magnitudes, and no single velocity dispersion is truly representative. Errors on the photometric parallaxes will also effect the partitioning of stars among the kinematic populations, as they propagate directly into errors on the tangential velocity. The magnitude of these effects could be estimated using suitable Monte Carlo models, however we have not done this here.

We also point out that while the moments of the velocity distribution can be recovered from proper motions alone (e.g. Dehnen & Binney 1998), reduced proper motion selected catalogues such as our own are most likely useless for measuring velocity distributions, due to the fact that the catalogue excludes low velocity stars.

9.3 A note on WDLF age estimates

The technique of dating a population of stars by measuring the position of the WDLF turnover has been applied successfully to young Galactic clusters. However, the position of the turnover is relatively insensitive to age at the canonical disk age of 8 Gyr, and it is the depth and structure beyond the turnover that is the main source of age constraint in this regime. This structure is still extremely uncertain for several reasons, including statistical error arising from the small numbers of stars and uncertain bolometric magnitudes for the ultracool white dwarfs that populate this range. Our work has shown that the different Galactic kinematic populations overlap significantly beyond the thin disk LF peak, and traditional approaches to the WDLF that do not allow for the possibility of a significant contribution from thick disk and spheroidal stars cannot hope to measure an accurate thin disk age. For these reasons it is our opinion that existing Galactic disk age measurements based on the WDLF turnover should be treated with caution.

Accurate aging of the kinematic populations separately would indeed be a major achievement of WD cosmochronology. This may have to wait for results from the PanSTARRS or Gaia surveys before the observational resources are in place. These would have to be matched by an improved understanding of the evolution and cooling times of the faintest white dwarfs, so that some of the current systematic errors (e.g. the spectral evolution problem) can be reduced.

ACKNOWLEDGMENTS

NR acknowledges the support of an STFC postgraduate studentship, which funded the majority of this work.

REFERENCES

- Bedin L. R., King I. R., Anderson J., Piotto G., Salaris M., Cassisi S., Serenelli A., 2008, *ApJ*, 678, 1279
- Bedin L. R., Salaris M., King I. R., Piotto G., Anderson J., Cassisi S., 2010, *ApJL*, 708, L32
- Bergeron P., Leggett S. K., 2002, *ApJ*, 580, 1070
- Bergeron P., Leggett S. K., Ruiz M. T., 2001, *ApJS*, 133, 413
- Bergeron P., Ruiz M. T., Hamuy M., Leggett S. K., Currie M. J., Lajoie C., Dufour P., 2005, *ApJ*, 625, 838
- Bessell M. S., 1986, *PASP*, 98, 1303
- Chiba M., Beers T. C., 2000, *AJ*, 119, 2843
- De Gennaro S., von Hippel T., Winget D. E., Kepler S. O., Nitta A., Koester D., Althaus L., 2008, *AJ*, 135, 1
- Dehnen W., Binney J. J., 1998, *MNRAS*, 298, 387
- Eisenstein D. J., Liebert J., Harris H. C., Kleinman S. J., Nitta A., Silvestri N., Anderson S. A., Barentine J. C., Brewington H. J., Brinkmann J., Harvanek M., Krzesiński J., Neilsen Jr. E. H., Long D., Schneider D. P., Snedden S. A., 2006, *ApJS*, 167, 40
- Evans D. W., 1989, *A&AS*, 78, 249
- Fontaine G., Brassard P., Bergeron P., 2001, *PASP*, 113, 409
- Fuchs B., Dettbarn C., Rix H., Beers T. C., Bizyaev D., Brewington H., Jahreiß H., Klement R., Malanushenko E., Malanushenko V., Oravetz D., Pan K., Simmons A., Snedden S., 2009, *AJ*, 137, 4149
- Gates E., Gyuk G., Harris H. C., Subbarao M., Anderson S., Kleinman S. J., Liebert J., Brewington H., Brinkmann J., Harvanek M., Krzesinski J., Lamb D. Q., Long D., Neilsen Jr. E. H., Newman P. R., Nitta A., Snedden S. A., 2004, *ApJL*, 612, L129
- Gehrels N., 1986, *ApJ*, 303, 336
- Geijo E. M., Torres S., Isern J., García-Berro E., 2006, *MNRAS*, 369, 1654
- Hambly N. C., Davenhall A. C., Irwin M. J., MacGillivray H. T., 2001, *MNRAS*
- Hambly N. C., Henry T. J., Subasavage J. P., Brown M. A., Jao W.-C., 2004, *AJ*, 128, 437
- Hambly N. C., Irwin M. J., MacGillivray H. T., 2001, *MNRAS*
- Hambly N. C., MacGillivray H. T., Read M. A., Tritton S. B., Thomson E. B., Kelly B. D., Morgan D. H., Smith R. E., Driver S. P., Williamson J., Parker Q. A., Hawkins M. R. S., Williams P. M., Lawrence A., 2001, *MNRAS*

- Hansen B. M. S., 1999, *ApJ*, 520, 680
- Hansen B. M. S., Brewer J., Fahlman G. G., Gibson B. K., Ibata R., Limongi M., Rich R. M., Richer H. B., Shara M. M., Stetson P. B., 2002, *ApJL*, 574, L155
- Hansen B. M. S., Liebert J., 2003, *ARA&A*, 41, 465
- Harris H. C., Dahn C. C., Vrba F. J., Henden A. A., Liebert J., Schmidt G. D., Reid I. N., 1999, *ApJ*, 524, 1000
- Harris H. C., Gates E., Gyuk G., Subbarao M., Anderson S. F., Hall P. B., Munn J. A., Liebert J., Knapp G. R., Bizyaev D., Malanushenko E., Malanushenko V., Pan K., Schneider D. P., Smith J. A., 2008, *ApJ*, 679, 697
- Harris H. C., Munn J. A., Kilic M., Liebert J., Williams K. A., von Hippel T., Levine S. E., Monet D. G., Eisenstein D. J., Kleinman S. J., et al. 2006, *AJ*, 131, 571
- Holberg J. B., 2009, *Journal of Physics Conference Series*, 172, 012022
- Jones L. R., Fong R., Shanks T., Ellis R. S., Peterson B. A., 1991, *MNRAS*, 249, 481
- Kilic M., Leggett S. K., Tremblay P., von Hippel T., Bergeron P., Harris H. C., Munn J. A., Williams K. A., Gates E., Farihi J., 2010, *ApJS*, 190, 77
- Kilic M., Munn J. A., Harris H. C., Liebert J., von Hippel T., Williams K. A., Metcalfe T. S., Winget D. E., Levine S. E., 2006, *AJ*, 131, 582
- Kilic M., Munn J. A., Williams K. A., Kowalski P. M., von Hippel T., Harris H. C., Jeffery E. J., DeGennaro S., Brown W. R., McLeod B., 2010, *ApJL*, 715, L21
- Knox R. A., Hawkins M. R. S., Hambly N. C., 1999, *MNRAS*, 306, 736
- Krzesinski J., Kleinman S. J., Nitta A., Hügelmeier S., Dreizler S., Liebert J., Harris H., 2009, *A&A*, 508, 339
- Lawson C. L., Hanson R. J., 1974, *Solving Least Squares Problems*. Prentice-Hall
- Leggett S. K., Ruiz M. T., Bergeron P., 1998, *ApJ*, 497, 294
- Liebert J., Bergeron P., Holberg J. B., 2005, *ApJS*, 156, 47
- Liebert J., Dahn C. C., Monet D. G., 1988, *ApJ*, 332, 891
- McMillan P. J., Binney J. J., 2009, *MNRAS*, 400, L103
- Mendez R. A., Guzman R., 1998, *A&A*, 333, 106
- Metcalfe N., Shanks T., Fong R., Jones L. R., 1991, *MNRAS*, 249, 498
- Murray C. A., 1983, *Vectorial Astrometry*. Taylor & Francis
- Oswalt T. D., Smith J. A., Wood M. A., Hintzen P., 1996, *Nature*, 382, 692
- Reed B. C., 2006, *JRASC*, 100, 146
- Reid I. N., 2005, *ARA&A*, 43, 247
- Robin A. C., Reylé C., Derrière S., Picaud S., 2003, *A&A*, 409, 523
- Rowell N. R., Kilic M., Hambly N. C., 2008, *MNRAS*, 385, L23
- Ruiz M. T., Bergeron P., 2001, *ApJ*, 558, 761
- Salim S., Rich R. M., Hansen B. M., Koopmans L. V. E., Oppenheimer B. R., Blandford R. D., 2004, *ApJ*, 601, 1075
- Savitzky A., Golay M. J. E., 1964, *Analytical Chemistry*, 36, 1627
- Schmidt M., 1968, *ApJ*, 151, 393
- Stobie R. S., Ishida K., Peacock J. A., 1989, *MNRAS*, 238, 709
- Tinney C. G., Reid I. N., Mould J. R., 1993, *ApJ*, 414, 254
- Tremblay P., Bergeron P., 2008, *ApJ*, 672, 1144
- Vidrih S., Bramich D. M., Hewett P. C., Evans N. W., Gilmore G., Hodgkin S., Smith M., Wyrzykowski L., Belokurov V., Fellhauer M., et al. 2007, *MNRAS*, 382, 515
- Winget D. E., Hansen C. J., Liebert J., van Horn H. M., Fontaine G., Nather R. E., Kepler S. O., Lamb D. Q., 1987, *ApJL*, 315, L77